ACSNANO

www.acsnano.org

ARTICLE

Signature Effects of Vector-Guided Systemic Nano Bioconjugate Delivery Across Blood-Brain Barrier of Normal, Alzheimer's, and Tumor Mouse Models

Liron L. Israel,[#] Anna Galstyan, Alysia Cox, Ekaterina S. Shatalova, Tao Sun, Mohammad-Harun Rashid, Zachary Grodzinski, Antonella Chiechi, Dieu-Trang Fuchs, Rameshwar Patil, Maya Koronyo-Hamaoui, Keith L. Black, Julia Y. Ljubimova,* and Eggehard Holler*

Cite This: *ACS Nano* 2022, 16, 11815–11832

Read Online

ACCESS | Metrics & More | Article Recommendations | Supporting Information

ABSTRACT: The ability to cross the blood-brain barrier (BBB) is critical for targeted therapy of the central nerve system (CNS). Six peptide vectors were covalently attached to a 50 kDa poly(β-L-malic acid)-trileucine polymer forming P/LLL(40%)/vector conjugates. The vectors were Angiopep-2 (AP2), B6, Miniap-4 (M4), and D-configurated peptides D1, D3, and ACI-89, with specificity for transcytosis receptors low-density lipoprotein receptor-related protein-1 (LRP-1), transferrin receptor (TfR), bee venom-derived ion channel, and Aβ/LRP-1 related transcytosis complex, respectively. The BBB-permeation efficacies were substantially increased ("boosted") in vector conjugates of P/LLL(40%). We have found that the copolymer group binds at the endothelial membrane and, by an allosterically membrane rearrangement, exposes the sites for vector−receptor complex formation. The specificity of vectors is indicated by competition experiments with nonconjugated vectors. P/LLL(40%) does not function as an inhibitor, suggesting that the copolymer binding site is eliminated after binding of the vector-nanoconjugate. The two-step mechanism, binding to endothelial membrane and allosteric exposure of transcytosis receptors, is supposed to be an integral feature of nanoconjugate-transcytosis pathways. *In vivo* brain delivery signatures of the nanoconjugates were recapitulated in mouse brains of normal, tumor (glioblastoma), and Alzheimer's disease (AD) models. BBB permeation of the tumor was most efficient, followed by normal and then AD-like brain. In tumor-bearing and normal brains, AP2 was the top performing vector; however, in AD models, D3 and D1 peptides were superior ones. The TfR vector B6 was equally efficient in normal and AD-model brains. Cross-permeation efficacies are manifested through modulated vector coligation and dosage escalation such as supra-linear dose dependence and crossover transcytosis activities.

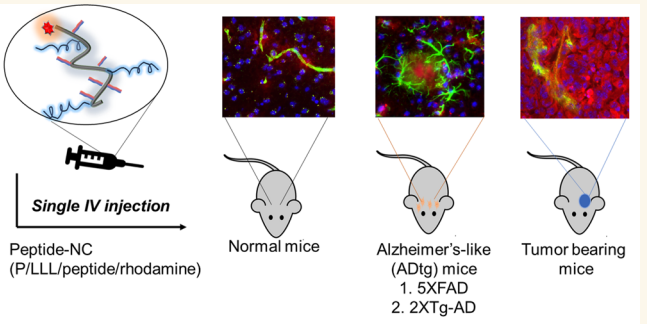

KEYWORDS: *blood-brain barrier, vector, receptor mediated transcytosis, brain tumor, Alzheimer's disease, shuttle peptides, nanocarriers*

Although essential for treatment of central nervous system (CNS) diseases, drug delivery through brain vascular endothelial layers is still underdeveloped due to the restriction by the BBB. Most pharmaceuticals and imaging agents require high doses to enter the brain that can result in off-target effects and systemic toxicity.[1−6] Among the reasons for insufficient BBB permeation are unfavorable large particle size, lack of targeting, and inappropriately high drug-receptor blocking binding affinities.[7] Moreover, previously achieved deliveries become ineffective due to disease-specific barrier tightening. For instance, in developing drugs for Alzheimer's disease (AD), transport across the BBB is disengaged by neuroinflammation and vascular amyloidosis.[8−13] In brain tumors, the extent of the enhanced permeability and retention (EPR) effect is marginal and not reproducible.[14,15] Failure of drug delivery could be fatal for

Received: November 11, 2021
Accepted: May 26, 2022
Published: August 12, 2022

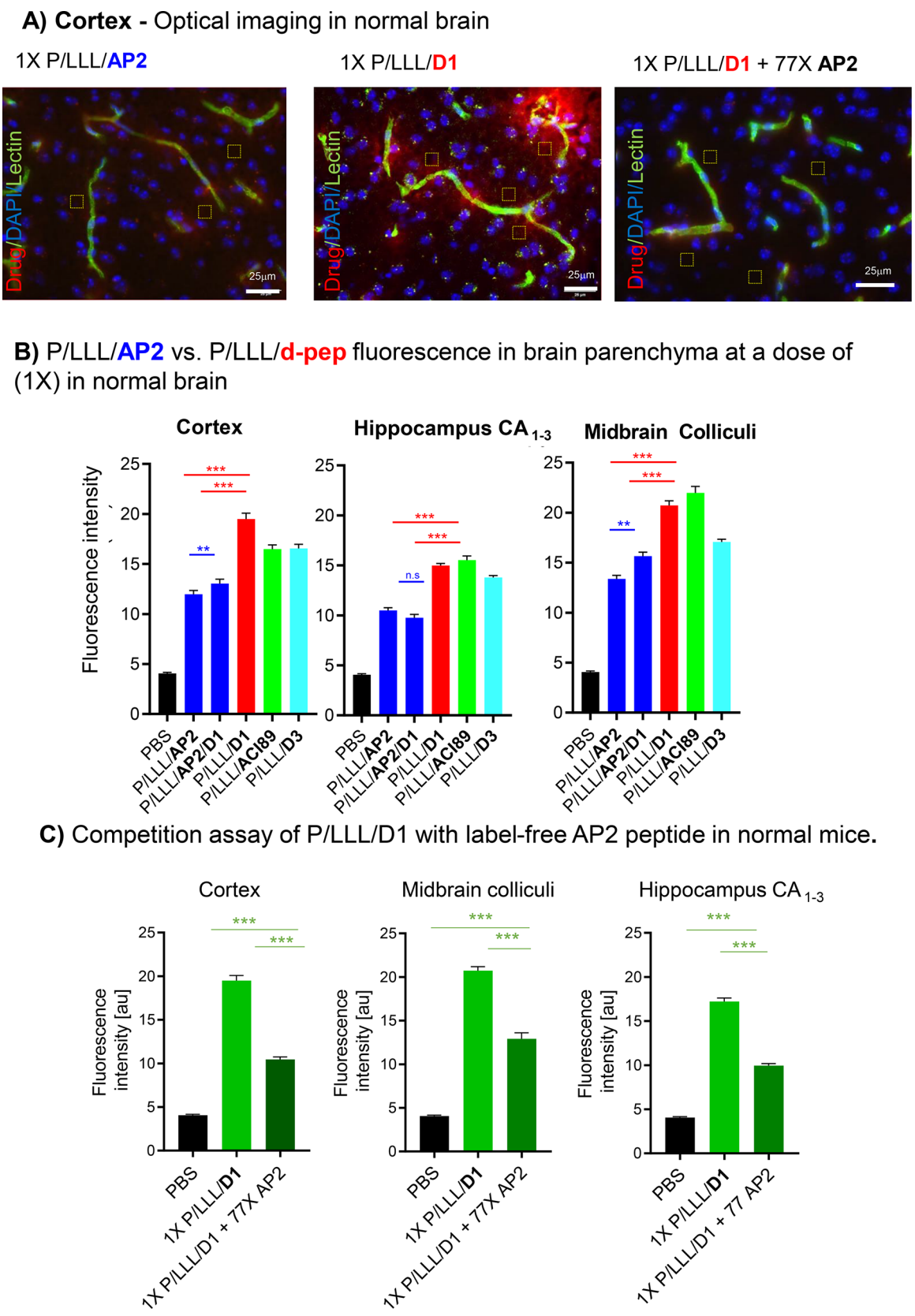

Figure 1. BBB-permeation in normal mice: the extent of BBB-penetration of nanoconjugates containing vectors AP2 or D-peptides functioning in the LRP1 pathway. All nanoconjugates are rhodamine labeled at the polymeric platform. (A) Optical imaging data showing fluorescence intensity as the indicator for the nanoconjugate permeation efficacy in the cerebral cortex of normal (healthy) brains. Nanoconjugate fluorescence is shown in red, the vasculature in green, and the cell nuclei in blue. (B) Average nanoconjugate fluorescence in layers II/III of the somatosensory cortex, the hippocampal CA1−3 cell layers, and the midbrain colliculi of normal mice. PBS background is shown in black, P/LLL/AP2 and P/LLL/AP2/D1 in blue, P/LLL/D1 in red, P/LLL/ACI89 in green, and P/LLL/D3 in cyan. (C)

https://doi.org/10.1021/acsnano.1c10034
ACS Nano 2022, 16, 11815−11832

Figure 1. continued

Competition with pristine (label-free) AP2. Average nanoconjugate fluorescence in layers II/III of the somatosensory cortex, the midbrain colliculi, and the hippocampal CA1−3 cell layers when coinjected with competitor AP2 (dark green), P/LLL/D1 injected alone (green), and compared to PBS (black). Average nanoconjugate fluorescence measurements were obtained from 20 randomly sampled regions of interest chosen outside of the cerebral vasculature (n = 3−4 with 3−4 images acquired from each mouse brain region). All statistical tests were conducted by one-way ANOVA with Tukey t tests using Prism. Statistical significance is indicated as follows: * = $p < 0.01$, ** = $p < 0.001$, and *** = $p < 0.0001$. Error bars represent SEM.

effective intervention.[2,16−18] Therefore, a knowledge of "personalized" delivery modalities is urgently needed.

The BBB is to a great extent managed by the endothelial cell layer of blood capillaries. Permeability is controlled by distinct pathways of *endo-* and *exo*-cytosis and of receptor-gated transcytosis. Examples for disease-modified transcytosis are specific receptors such as LRP-1 and TfR that mediate the transfer through the BBB. In some AD model mice, the LRP-1 receptor is downregulated in comparison to the healthy brain, while TfR levels remain unchanged.[19−25] In glioblastoma multiforme, a fast-growing brain tumor, both LRP-1 and TfR are upregulated. In AD, upregulated receptor for advanced glycation end products (RAGE) mediates an increased level of amyloid-β (Aβ) peptides in the brain. This upregulation, along with pericyte loss and/or the age-dependent decline of microvascular LRP-1, contributes to AD progression in mice.[26−29] Furthermore, the over-reaching effect of enhanced levels of Aβ in AD may affect the transcytosis activity of LRP-1 for vector-dependent drug delivery to the brain. Another potentially interconnecting system involving the transport of amino acid or analogues across the brain vasculature endothelia is the highly expressed large neutral amino acid transporter (LAT-1).[30−37] Additionally, dysregulated tight junctions (TJ) between the vascular endothelial cells could not yet be ruled out as a source of brain disease and factors in altered pharmaceutical delivery to the brain during AD progression.[38,39]

In the forefront of possible disease-mediated interconnections between endothelium pathways through the BBB, we considered the design of a universally applicable delivery platform in the study of disease mechanisms and treatments.[40] Here, we chose the copolymer (β-L-malic acid/40% trileucine), P/LLL(40%), which has been used as a platform in drug delivery to treat various brain and breast tumors.[24,40−43] The polymer has a balanced hydrophobic/lipophilic composition and binds to and interacts with hydrophobic constituents of cellular and vesicle membranes.[42,43] We consider the polymer-trileucine group as amphiphilic which contains multiple carboxylic groups for vector-receptor attachment and, moreover, can be biodegraded by lipases and peptidases and thereby escape deposit toxicity *in vivo*. Borderline nanopolymer platforms are experimentally available for deep tissue penetration and rapid renal clearance.[44]

After systemic intravenous (IV) injection, labeled platform−vector conjugates were tracked by quantitative fluorescence microscopy (Figure S1).[40] The tracked intensities after migration from brain microvessels into the parenchyma was measured in both normal and diseased mouse brains in order to derive specific BBB permeation signatures. In particular, it would be of interest if platform-loading with multiple vectors owning different specificities could provoke variations in permeation efficacy and brain location. Experiments with vectors targeting distinct permeation pathways could give information on networks and their regulation. Investigated vectors and receptors are the following: (1) Angiopep-2 (AP2) of the LRP-1[19,45−49] pathway with receptor affinity to amyloid precursor protein (APP)[50] and Aβ_{1-40} and Aβ_{1-42}[51] peptides as well as D-peptides[52,53] sharing specific recognition of amyloid peptides Aβ_{1-40}, Aβ_{1-42}, Aβ-fibrils,[54] Aβ plaques,[55] or fibril-free diffuse Aβ aggregates;[56] (2) B6-peptide with specificity for the TfR-pathway;[34,57−61] and (3) Miniap-4 (M4) vector with specificity for Apamin (bee venom)-derived potassium channel, which has previously been shown top be active in BBB permeation but without markedly affecting pathological conditions.[62−66] (4) We have also included platform P/LLL(40%) in order to shed light on its ability to permeate BBB and boost these vectors.[40]

A signature for AD was found in the reduction of BBB permeation by comparison of LRP-1 shuttle peptides in AD mouse models. To provide a background, a search was conducted by RNA-*Seq* analysis for unmasking variations involved in AD metabolism caused by the dysregulation of gene expression in their CNS location. In this context, we examined interconnections between BBB transcytosis pathways, especially prominent in AD increased brain distribution of Aβ-peptides, which is out of balance in AD by the RAGE- and LAT-1 pathways and could possibly be combated by the treatment with LRP1 active D-peptide vectors.[1,53]

In vitro Transwell BBB permeation consisting of human microvascular endothelial cells was used for deepening the study on possible mechanisms of normal and AD-like brains and to shed light on the intriguing *in vivo* permeation results. Clearly, dysregulation of gene expression at the brain-blood barrier interface is of importance for the understanding of disease-specific mechanisms and their contribution to treatments of neurological disorders.

RESULTS AND DISCUSSION

BBB Crossing Involving AP2 Vector Binding Sites in Normal Brain and in Transwell Microvascular Endothelial Cell Layer BBB Model. The conjugates of P/LLL(40%) with vectors M4, AP2, and B6 (Table S1) were previously shown to achieve high brain permeation in the cortex and midbrain but only a fraction of delivery in the hippocampus.[40] Neither free rhodamine nor poly(malic acid−rhodamine) conjugate controls at doses as high as 2X exhibited fluorescence penetrating into the parenchyma ruled out unspecific results.[40] Brain sections in Figure 1A display the red fluorescence of the vector conjugates appearing in the parenchyma. In bar graphs (Figure 1B), the fluorescence intensity (BBB-permeation efficacies) for P/LLL/AP2, P/LLL/AP2/D1, P/LLL/D1, P/LLL/ACI89, and P/LLL/D3 were grouped according their locations in cortex layer II/III, hippocampus, and midbrain colliculi. The fluorescence intensities (permeation efficacies) varied with the vector type, increased linearly with low doses (0.25X−1X) (0.25X = 0.068 μmol/kg), and deviated from linearity toward higher efficacies at high doses.[40] The permeation efficacies of P/LLL/

https://doi.org/10.1021/acsnano.1c10034
ACS Nano 2022, 16, 11815−11832

Table 1. Transwell Inhibition Experiments[a]

	percent ± SEM of BBB-permeability remaining in the presence of competitor		
nanoconjugate	JPH203 ± SEM	$A\beta_{1-40}$	AP2 ± SEM
P/LLL	111 ± 3 (0.213, ns)	-	80 ± 2 (0.045, *)
P/LLL/D3	80 ± 2 (0.0009, ***)	30 ± 4 (0.0005, ***)	66 ± 4 (0.0005, ***)
P/LLL/AP2	58 ± 5 (0.016, *)	41 ± 8 (0.007, **)	-

[a]Permeability competition experiments using the *in vitro* Transwell model of the BBB. Permeation through the model was measured by fluorescence intensity in the target compartment. Competition is indicated by the relative fluorescence decrease in the presence of the tested compound. (1) D3-nanoconjugate inhibition by AP2. (2) AP2- and D3-nanoconjugate inhibition by Aβ.[16,35] (3) AP2- and D3-conjugate inhibition by inhibition with the LAT-1 specific inhibitor JPH203.[73] (4) P/LLL(40%) by marginal inhibition with AP2. P/LLL(40%), the nanoconjugate platform, served as a control. *$p < 0.05$, **$p < 0.01$, ***$p < 0.001$, Student's t test comparing compounds in the presence and absence of inhibitor. The mode of inhibition, competitive or noncompetitive, was not determined.

AP2/D1 (right blue), P/LLL/D1 (red), P/LLL/D3 (turquoise), and P/LLL/AC189 (green) exceed that of P/LLL/AP2 (left blue bar) at the given dose 1X (1X = 0.272 μmol/kg). In addition, it was noted that the simultaneous loading of AP2 and D1 in P/LLL/AP2/D1 (Figure 1B) resulted in significantly less fluorescence intensity, not accounting for the sum of contributions P/LLL/AP2 and P/LLL/D1. The effects were considered sensitive to the composition of the loaded vector-nanoconjugates. They could indicate structural constraints originating from vector geometrical arrangements and/or allosteric mechanisms of receptor binding.

To gain further insight in the vector-conjugate BBB-permeation mechanism, the Transwell BBB system was chosen. It was thought that this model assay was less complicated due to possible direct manipulations that were more complex than in the animal systems. The goal was to examine the polymer platform P/LLL(40%) and the vector group contributions by competition experiments.[67] We compared the permeation at 0.25X dose (Figure S2, Table S2, TEER-Figure S3) for Transwell experiments decreasing in the order P/LLL/AP2 > P/LLL/M4 > P/LLL/B6 in Figure S2 (range of 2.05×10^{-3} cm/min to 8.0×10^{-3} cm/min) with results[40] for *in vivo* experiments in Figure 1C (midbrain colliculi[40]) under the same concentration conditions. A full agreement was not expected because the origin of endothelial cells and the setup were different. Importantly, the overall permeation variations in the two systems were similar. To identify functional relations between nanoconjugate vectors AP2, B6, M4, D-peptides (D1, D3), amyloid peptides, and the LAT-1 specific inhibitor JPH203, Transwell and *in vivo* competition experiments were carried out.

D-Peptides *In Vivo* Transfer across the BBB by the AP2-Pathway, Relevance to AD-Associated Aβ Alloforms. D-Peptide(vector)-nanoconjugates displayed *in vivo* permeabilities that were superior to those of AP2-nanoconjugates in normal brain at the given dose (Figure 1B). A BBB-crossing mechanism common for Ap2 and the D-peptides was sought as an explanation that contained specific patterns which enabled superior BBB-permeation of the D-peptides. AP2 is the signature vector of the LRP1 transcytosis pathway through vascular endothelia of normal brain.[40,46] Evidence that AP2 as well as the D-peptides target Aβ and Aβ-deposits[50] suggested already that these vectors transferred through the LRP1 pathway which was also known to transport precursor APP and amyloid peptides.[9−51] In support for this hypothesis, the decrease in fluorescence intensity verified a shared receptor by demonstration of the *in vivo* decrease for P/LLL/D1 by administering free AP2 peptide in a 77-fold higher dose (Figure 1A, right panel; C). Next, the Transwell assay also demonstrated competitive sharing of P/LLL/D3 with AP2 (Table 1) in line with AP2, D1, and D3 sharing the transcytosis pathway. Another mechanism for the D1- and D3-peptide vectors was recently assumed which involved adsorptive-mediated transcytosis, consistent with the presence of positive charges in the D1 and D3 vectors that can bind the negatively charged endothelial membrane.[68] According to our results, this mechanism is not consistent with the observed AP2 and D1- and D3-nanoconjugate competition pathway. A deviation of the adsorptive transcytosis pathway could be explained by the overriding highly negative zeta-potential of −11 mV[40] of PMLA(LLL(40%) over the positive charges of D1 (qshyrhispaqv, 3+)[54] and D3 (rprtrlhthrnr, 7+).[55] If the adsorptive mechanism is in place for the free vectors, the modulating influence of the P/LLL(40%) platform is an example of possible platform-induced variations.

Recalling that AP2 and D-peptides have affinity for Aβ binding,[53−55] and that LRP1 is known to transport APP and Aβ species across the BBB, we may implement another crossing of receptor binding. Again, a competition assay with the Transwell resolved that effects of $A\beta_{1-40}$[26,68] on the permeation of P/LLL/D3, P/LLL/AP2, and P/LLL(40%) through cells was found under both normal and pathological conditions. Under the condition of the Transwell assay, BBB-permeation of both P/LLL/D3 and P/LLL/AP2 was inhibited by $A\beta_{1-40}$ in agreement with its transcytosis via the LRP-1 pathway[26,68] (Table 1), substantiated further by the *in vivo* inhibition experiment of the D1-nanoconjugate by AP2 (Figure 1C) attesting LRP1 binding sites functioning for AP2 and D-peptides under *in vivo* and *in vitro* conditions.

Transwell Support of AP2-Vector Independent Binding Sites for P/LLL/B6 and P/LLL/M4. An open question of interest was whether pristine (free) AP2 vector could also bind to receptor sites for B6 and M4 vector-P/LLL(40%) conjugates. In the Transwell system, the vector-conjugates did not reveal inhibition by free AP2 (Figure S4) in agreement with the absence of cross-reactivity of AP2 with binding sites on M4- or B6-transcytosis receptors.

AP2-Vector Site Interaction with LAT-1 Inhibitor JPH203. We also tested whether the Transwell system could be sensitive to competition of P/LLL/D3 and P/LLL/AP by JPH203, an inhibitor of the LAT-1 pathway (which is a member of the Solute Carrier family or SLC 7a5). Indeed, the LAT-1 inhibitor was active against the permeation of the tested conjugates (Table 1). The transporter could have specificity for amino acids such as tyrosine and phenylalanine in the N-terminal region of AP2-peptide. The binding of P/LLL/D3 and P/LLL/AP to the transporter appears not unlikely in light

https://doi.org/10.1021/acsnano.1c10034
ACS Nano 2022, 16, 11815−11832

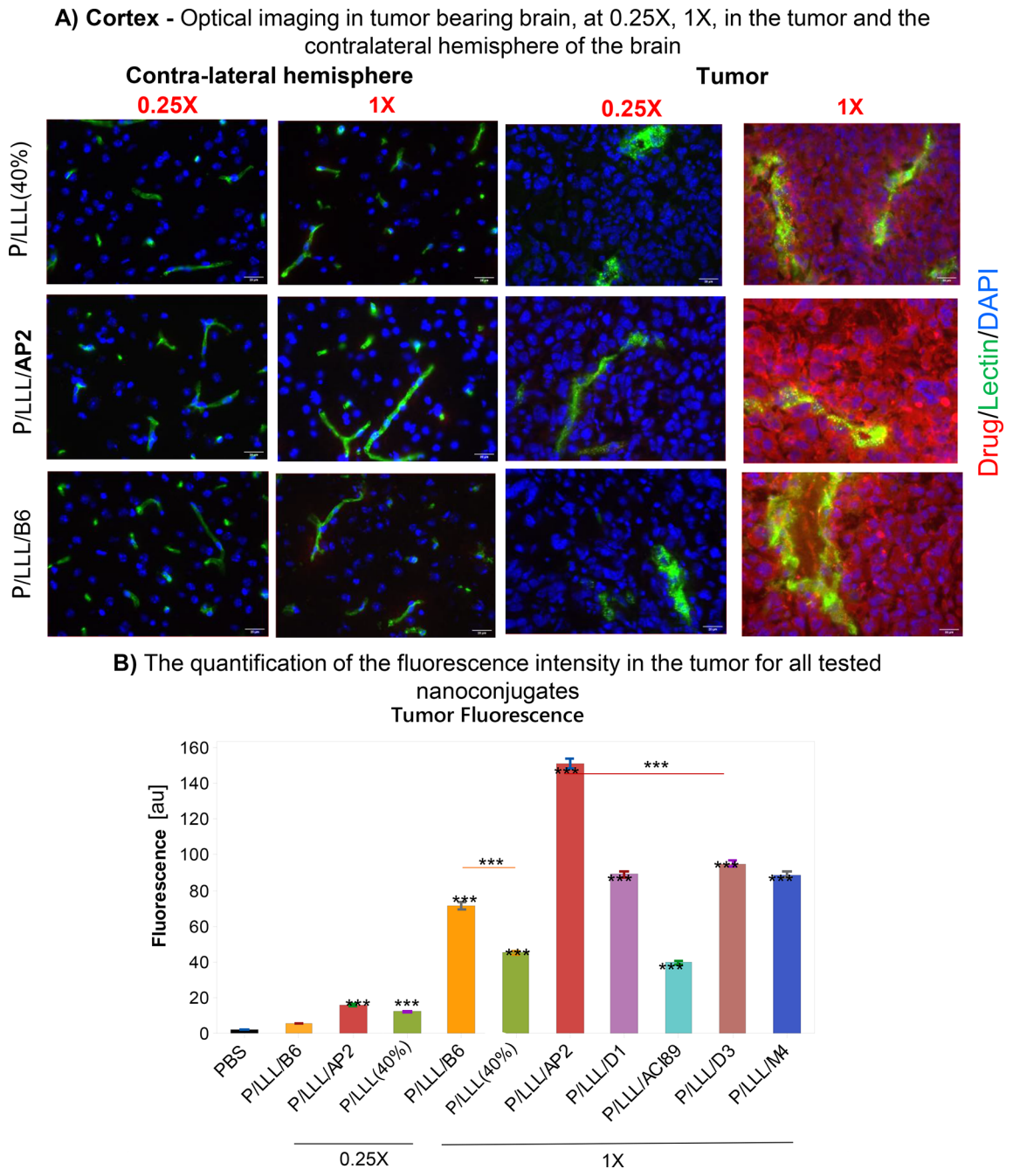

Figure 2. BBB-permeation in brain tumor: Imaging and tumor permeation analysis in a mouse model of glioblastoma. Female BL/6 Mice (n = 3) were inoculated intracranially with glioblastoma cell line GL261 at 8 weeks of age and measured 3 weeks after inoculation. A comparison of the permeability of P/LLL(40%), P/LLLAP2, P/LLLB6, P/LLL/D1, P/LLL/AC189, P/LLL/D3, and P/LLL/M4 in tumor and nontumor tissue from the contralateral brain hemisphere was carried out. (A) Representative optical imaging data showing nanoconjugate permeation into the tumor (right) and in the cerebral cortex of the contralateral hemisphere in the same animal (left). Comparison of dose 0.25X (0.068 μmol/kg) and dose 1X (0.274 μmol/kg). Nanoconjugate fluorescence (red), vasculature (green), and cell nuclei (blue) are shown. (B) Intensity bar-graph for nanoconjugate fluorescence in tumor tissue. Background is shown in black, P/LLL(40%) (0.25X and 1X) in green, P/LLL/B6 (0.25X and 1X) in orange, P/LLL/AP2 (0.25X and 1X) in red, P/LLL/D1 (1X) in violet, P/LLL/ACI89 (1X) in blue, P/LLL/D3 (1X) in brown, and P/LLL/M4 (1X) in dark blue. Average nanoconjugate fluorescence measurements were obtained from 20 randomly sampled ROIs outside of the cerebral vasculature (n = 3 with 5 images acquired in each tumor and nontumor tissue sample). All statistical tests were conducted by one-way ANOVA with Tukey t tests. Significance is indicated with asterisks where * = p < 0.01, ** = p < 0.001, and *** = p < 0.0001. Error bars represent SEM.

of reported high expression in brain endothelial cells[18] and brain tumors.[36,69−72]

BBB Permeation in the Murine *Syngeneic* Glioblastoma GL-261 Tumor Model. In glioblastoma brains, BBB disruption enables high uptake of nutrient and growth promoting factors,[15−18] especially in GL-261 glioblastoma as an aggressive and fast-growing tumor. Three weeks after intracranial inoculation of BL/6 mice with GL261 cells, rhodamine-labeled nanoconjugates were IV-injected and animals sacrificed 2 h post-injection. BBB permeation efficacies

https://doi.org/10.1021/acsnano.1c10034
ACS Nano 2022, 16, 11815−11832

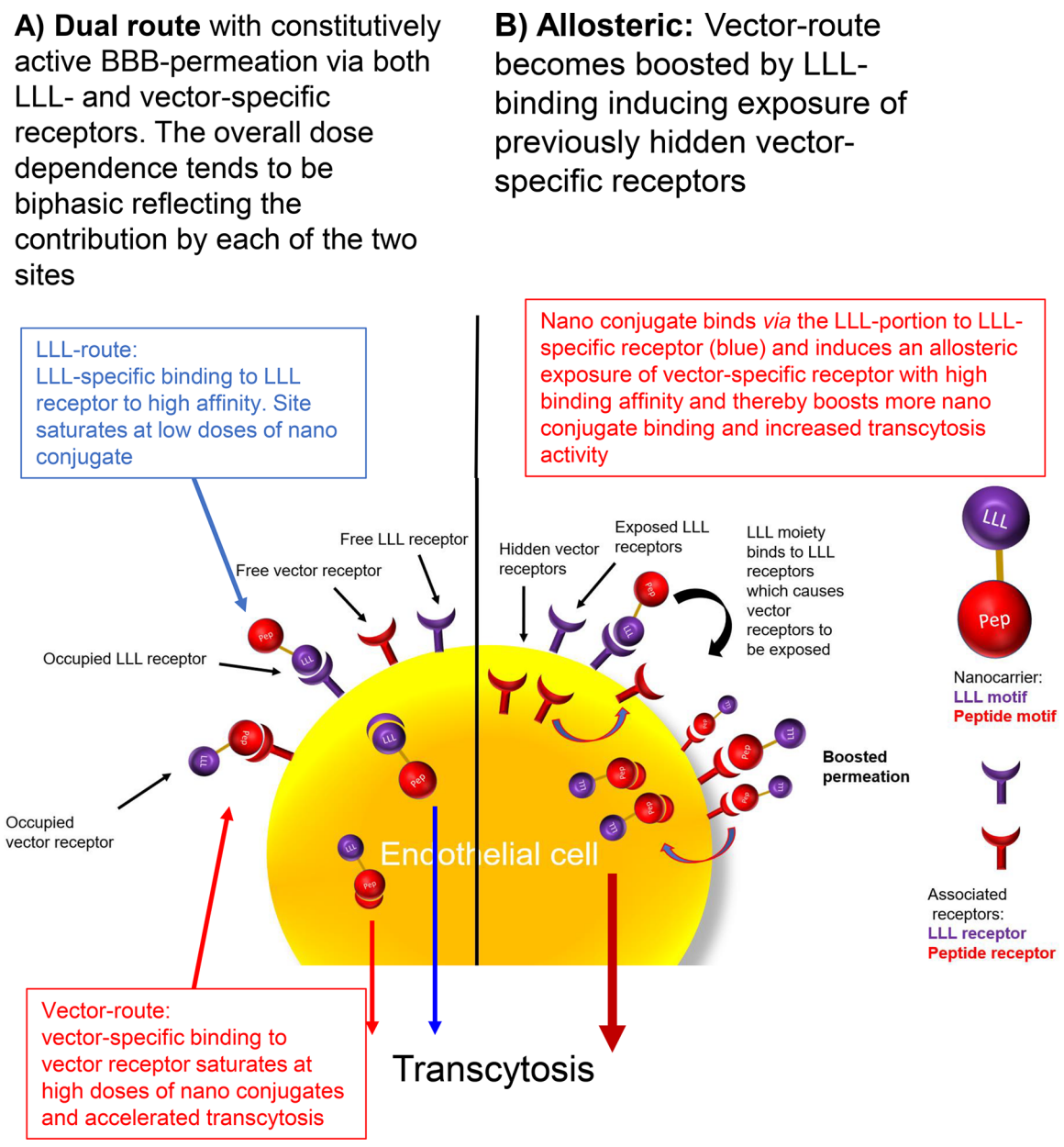

Figure 3. BBB-permeation mechanisms of P/LLL(40%) (purple) and P/LLL(40%)/vector (red). LLL refers to P/LLL(40%). (A) Suggested dual constitutive mechanism. The LLL-portion and the vector-portion of the nanoconjugates bind freely to the LLL-specific receptor (blue) and the vector-specific receptor (red), respectively, on the surface of the endothelial membrane. Both receptors ferry the bound ligands through BBB, and the combined results would indicate that the permeation efficacy is additive. (B) Each of the LLL and vector portions of the nanoconjugates bind to independent receptors and proceed directly to transcytosis as shown in (A). However, in mechanism B, the binding of the LLL-portion would allosterically induce the exposure of receptor sites previously hidden inaccessible in the membrane, and a "boost" phenomenon is observed. While the receptor remains exposed, it carries out one or more rounds of vector binding and transcytosis. Thereby, the BBB-permeation efficacy could be increased in comparison with the constitutional system (mechanism A) and is manifested as the "boost" phenomenon. If multiple LLL-binding sites contribute to boosted BBB-permeability, the permeation efficacy is likely to follow a supra-linear dose dependence. Moreover, binding of free P/LLL(40%) molecules would not function as competitive inhibitors but rather as BBB-permeation activators. The indication of "boosts", supra-linear dose dependence, and insensitivity against the competition are hallmarks of the BBB permeation by the P/LLL/vector conjugate.

were analyzed in sections of both tumor tissue and nontumor tissue in the contralateral brain hemisphere (Figures 2A, S6A). The fluorescence intensity in tumor tissue after nanoconjugates was very high in comparison to that in nontumor tissue. In order to compare brain tumor tissue containing extremely high and low fluorescence intensities, fixation and washing together with a shortened imaging were adapted in a standard protocol to yield acceptable signal-to-noise ratios.

Results in the bar graph Figure 2B were obtained with the adapted protocol. (i) The very high permeation efficacies at dose 1.0X are compared as a function of the type of vector. The bar-value for P/LLL/AP2 is the highest, followed by P/LLL/D3, P/LLL/M4, P/LLL/D1, P/LLL/B6, P/LLL(40%), and P/LLL/AC189. (ii) A supra-linear increase from doses 0.25X to dose 1.0X is demonstrated for P/LLL/B6 (23-fold) and P/LLL/AP2 (11.2-fold). (iii) An exemption is P/

https://doi.org/10.1021/acsnano.1c10034
ACS Nano 2022, 16, 11815−11832

LLL(40%), which increases proportionally with the dose administered.

Supra-Linear Dose Dependence and the "Boost" Phenomenon. The origin of supra-linearity was considered to be related to the "boost" in BBB-permeation efficacy exhibited when introducing the conjugation of 40% of the pendant polymer-COOH residues with tri(L-leucine).[40] Non-linearity is in agreement with an allosteric kinetic model and the cooperativity manifested by the observed "boost" (Figure 3B). Combining low and high affinity binding sites (Figure 3A) as an explanation would generate a "bumpy" dose dependence which was not observed. The mechanism of an allosteric cooperative model combines binding of the P/LLL(40%) portion at an effector site followed by binding of the vector portion at the site which is productive in transcytosis (Figure 3B). The coupling of P/LLL(40%) at the first site functions to activate the transcytosis by an allosteric rearrangement. Competition of P/LLL(40%) at the activator site had no effect on P/LLL/AP2 (Figure S5) indicating that the site was inactive in the presence of the P/LLL(40%)/AP2 vector-complex. Similar results were obtained by the Transwell method concluding the absence of competition between the nanoconjugates carrying B6 or M4 and P/LLL(40%) (Figure S4). *In vivo* experiments provided results that the effector site is available and does not interfere with transcytosis, but rather increases the boosting shown in the case of P/LLL/B6 transcytosis (Figure S5). This could indicate that the allosteric change can depend on the structure of the nanoconjugate undergoing transcytosis. Supporting evidence for a possibly deep structural change is in accord with the observation that P/LLL(40%) can induce membrane leakiness.[42,43]

In the present situation, a simple working model is favored, where the P/LLL-vector binds to abundant sites on the surface of membranes in the environment of a receptor and provokes structure rearrangements which render membrane-imbedded receptors accessible to P/LLL(40%)/vectors, while the effector portion is buried in the membrane. The location of multiple effector sites around receptors resembles multiple substrate binding sites of enzymes showing cooperativity. By this token, the mechanism could explain the supra-linear efficacy as a function of dose. The allosteric mechanism could be susceptible to biospecific parameters (i) density and distribution of P/LLL(40%) sites around receptor sites, (ii) variations in structure specific affinities of membrane and receptor binding, (iii) interfering interactions by fixed pathway-specific components or competitive mobile ligands, and (iv) brain-status and disease-specific interactions.

In glioblastoma, a boost-favoring nanoconjugate could promote tumor (T) uptake over nontumor normal brain (NB) characterized by T/NB ratio in Table S3. The depicted examples indicate selectivity for the platform conjugates P/LLL/AP2, T/NB(0.25X) = 6.5, and T/NB(1X) = 15.7; vector P/LLL/B6, T/NB(1X) = 10.2; vector P/LLL/M4, T/NB(1X) of 22.8; and vector P/LLL/D1, T/NB(1X) = 16.4. The effector platform P/LLL(40%) itself produced modest selectivity at dose 0.25X (T/NB = 8.3) (0.25X) and dose 1X (T/NB = 9.7). In summary, the selectivity is indicated by (i) the boosting inferred by P/LLL(40%)-moiety and (ii) the supra-linear dose dependence. Both are signatures of the platform−vector conjugates. Much less boosting and supra-linear dose effect were seen in normal brain[40] and in AD brain (data below). It is hypothesized that external effectors, tumor endothelial vasculature specifics, in particular, the expression levels of transcytosis receptors,[20,21] translate via the discussed parameters into different signatures. The P/LLL(40%) contribution may count as a special feature in our investigation; however, it may represent a not yet recognized natural player. The interesting high selectivity for M4 deserves further investigation.

Multiparameter Factorial Analysis Further Explicates the Composition of Receptor Complexes, BBB-Permeation Efficiency, and Tumor Selectivity. To shed more light on the complexity of receptor−ligand complexes in BBB-permeation, we considered in more detail the interconnection in tumor-brain between binding to the P/LLL(40%) membrane sites and the vectors binding to the transcytosis pathway receptor site BBB permeation: We have shown that P/LLL(40%) alone penetrates BBB in the absence of vectors, although at low efficacy, and also that vectors AP2 (and their derivatives D1, D3, ACI89), and vectors B6, M4 penetrate BBB in the absence of conjugated P/LLL(40%) (the receptor-pathway), although at low efficacy.[40] We have also shown that free vectors and other molecules which bind to the receptor-vector sites disrupt the high-efficacy permeation pathway indicating that they have access to the transcytosis pathways and can function in their pathway regulation.

In an extension of the site-coupling P/LLL(40%) with the constitutive vectors AP2, M4, B6, and D1, we examined whether coupling between vectors−vectors in the nanoconjugate load could be possible. Indeed, effects of coligation of vectors have been shown to restrict permeability in examples of AP2 and M4, or AP2 and D1 coligation.[40] We also examined whether activation could be possible (1), whether effects could be (2) tuned by the number of different coligated vectors, and (3) whether coloading effects were sensitive to variations in the administered dose of the injected P/LLL(40%) vector.. To study multivariable experiments, we launched a "factorial study" analysis[74−76] (DoE, Design of Experiment, Supporting Information). As an example, we chose BBB permeation of P/LLL/AP2 in tumor-bearing brains (Case 1. Single vector, Table 2A), in comparison with P/LLL/AP2/B6 at varied dosage (Case 2. Co-ligated vectors AP2 and B6 tested in tumor and normal brain of the same animal, Table 2B); fluorescence permeation into the tumor (response T), into the nontumor brain (NT), and the tumor selectivity (response T/NT) were evaluated. The DoE experimental matrices are summarized in Table 2. For further technical details, see Materials and Methods.

Inspection of the contour plots shows that the region of the highest tumor selectivity contains the region of highest loading dose 1X (yellow arrows in Figure 4A,B). The presence of B6-peptide (Case 2) enhances selectivity in the region of the center point (Figure 4B) for 0.625X, 1% AP2, green arrow, and reduces selectivity at lower doses (Figure 4B), white arrow at 0.375X, 1% AP2. Doses below 0.375X AP2 effect lower selectivity for the combined AP2/B6 nanoconjugate (Figure 4B) than for P/LLL/AP2 (1X) (Figure 4A). At 0.25X AP2, selectivity for P/LLL(40%)/AP2(0%)/B6(2%) (Figure 4B) is less than in Figure 4A at 0.25X for P/LLL/AP2(0%). Selectivity T/NB > 12 cannot be achieved for nanoconjugates P/LLL/AP2 in the range 0.25X−1X (Figure 4A). This selectivity is only achieved by coattachment of AP2 and B6 in the nanoconjugate P/LLL/B6(1%)/AP2(1%) and at a dose close to 0.625X (Figure 4B). The contour plots indicate also that favorable T/NB in the range 12−14 extends from

https://doi.org/10.1021/acsnano.1c10034
ACS Nano 2022, 16, 11815−11832

Table 2. Factorial Study on Tumor-Bearing BL/6 Mice[a]

2A AP2-Matrix			
Factor: AP2-loading (% coligation of AP2)	Factor: Dose [X]	Response (1): Fluorescence intensity (uptake in tumor)	Response (2): Tumor Selectivity (ratio T/NB)
0	0.25	10.02	9.73
1	0.625	31.20	11.87
2	0.25	13.48	6.51
2	1	148.25	15.75
0	1	42.66	5.13

2B Combined Matrix				
Factor: AP2-loading (% AP2 = 2%−X%B6)	Factor: B6 B6-loading (%B6 = 2%−X%AP2)	Factor: Dose [X]	Response (1): Fluorescence intensity (uptake in tumor)	Response (2): Tumor Selectivity (ratio T/NB)
2	0	0.25	13.48	6.55
1	1	0.625	50.39	12.17
0	2	1	69.20	10.25
2	0	1	148.25	15.75
0	2	0.25	2.97	6.84

[a]DoE-matrix which contains factor "loading AP2" or factor "loading AP2, B6", factor "DoseX", the response (1) "Fluorescence Intensity" and response tumor (2) "Selectivity".

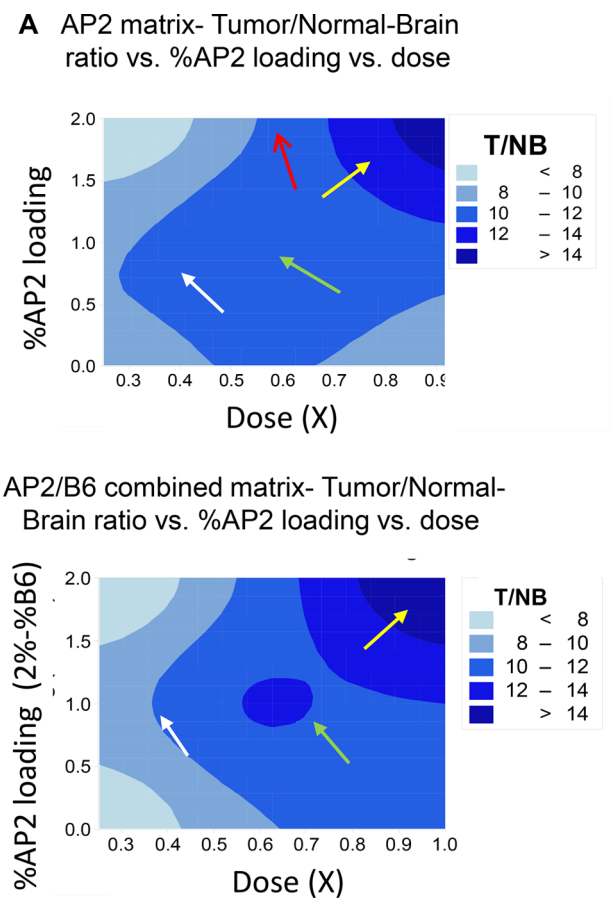

Figure 4. Factorial study: 2D contour plots for the selectivity response T/NB ratio (dosage is shown on X-axis, % AP2 loading is shown on *Y*-axis, and T/NB ratio is shown on *Z*-axis). (A) represents the single peptide-matrix (P/LLL/AP2), and (B) represents the combined peptide-matrix (P/LLL/AP2/B6). For more details, see Supporting Information.

AP2(1.5%) to AP2(1.0%) range 0.75X−0.9X and the presence of coligand B6 (Figure 4B) in comparison with the AP2(1.5%) to AP2 (1.2%) range 7.5X−0.9X and the absence of B6 (Figure 4A). This indicates that coligation of B6 intensifies the selectivity of the AP2, B6-coloaded nanoconjugate for tumor delivery. The DoE-generated "significance"-plots ("Pareto chart", Figure S6B1,B2), and "interaction"-plots (Figure S6B1,B2) strengthen the statistical significance of the analysis and demonstrate coupling between the coligated vectors AP2 and B6. An in-depth analysis is available in the Supporting Information. In summary, the examples present evidence for a multiplicity of allosteric positive and negative coupling routes between transcytosis pathways of LRP1 and TfR when AP2 and B6 were physically connected via coloading on platform P/LLL(40%). Depending on their percentage and stoichiometry, the AP2- and B6-vectors yielded various dose-dependent nanoconjugate−receptor complexes with alternating preferences for normal or brain tumor regions.

BBB Crossing in AD Mouse Models: 5XFAD and 2XTg-AD. The condition of brain vascular endothelium is investigated in two mouse models of AD. By comparing the permeability of nanoconjugates in the healthy brain, tumor-bearing brain, and AD-like brain of mice, we can characterize this third status as a constraint type of BBB.[8−10] Research suggests that in AD dementia, certain brain changes such as Aβ accumulation may begin 20 or more years before AD symptoms appear.[77−84] In this prodromal phase, subtle changes in gene expression occur; one of them is down-regulation of LRP1,[19] while TfR expression is unaffected.[85] Here, we probed BBB in the permeability of nanoconjugates in normal mouse brains compared to two transgenic mouse models of AD (ADtg).

BBB permeability in (i) double transgenic (2XTg) mice [6−8-month-old mixed gender, B6.Cg-Tg ($APP_{SWE}/PS1_{\Delta E9}$)-85Dbo/Mmjax] using nanoconjugates P/LLL/D1, P/LLL/D3, and in (ii) 5XFAD mice [B6.Cg-Tg(APPSwFlLon, PSEN1*M146L*L286 V)6799Vas/Mmjax], which contained two transgenes and three mutations within APP and PSEN1 genes known to accelerate disease progression, using nanoconjugates P/LLL/AP2, P/LLL/B6, P/LLL/M4, P/LLL/D3, and P/LLL/D1. In 5XFAD mice, dosage had to be increased from 1X in normal brain[40] to 2X in order to obtain acceptable readings of fluorescence intensities in the hippocampus and the cortex reflecting the tightened status of the AD-brain (Figure 5A). The averaged intensity bar-plots (not corrected for background intensities) are shown in Figure 5B,C. The bar-heights in these plots appear to be "scrambled" missing an ordered dependence previously noted for normal brain. Thus, permeation efficacy ratios for 5XFAD over normal are 0.42 (P/LLL/AP2), 0.82 (P/LLL/D3), and 0.68 (P/LLL(40%). The ratio 1.1 for P/LLL/B6 is an indication of the conserved expression of TfR, whereas the low ratios for AP2, D3 are in agreement with the downregulation of LRP-1.[85] The bar plots for 2XTg mice are shown in Figure 5D,E. The low permeation efficacy indicated in panels D and E at doses <2X is considered a BBB-signature at low dose in ADtg mice. At the dose of 2X, high permeations for D1 and D3 conjugates pop up in 2XTg-AD mice and similar but less pronounced in 5XFAD mice. This abrupt increase afforded a mechanism based on the disease and is discussed in the following section.

Suppression of Nanoconjugate Permeability in AD Invoked by Upregulation of RAGE. The observed restriction in 2XTg-AD mouse BBB permeability was explained

https://doi.org/10.1021/acsnano.1c10034
ACS Nano 2022, 16, 11815−11832

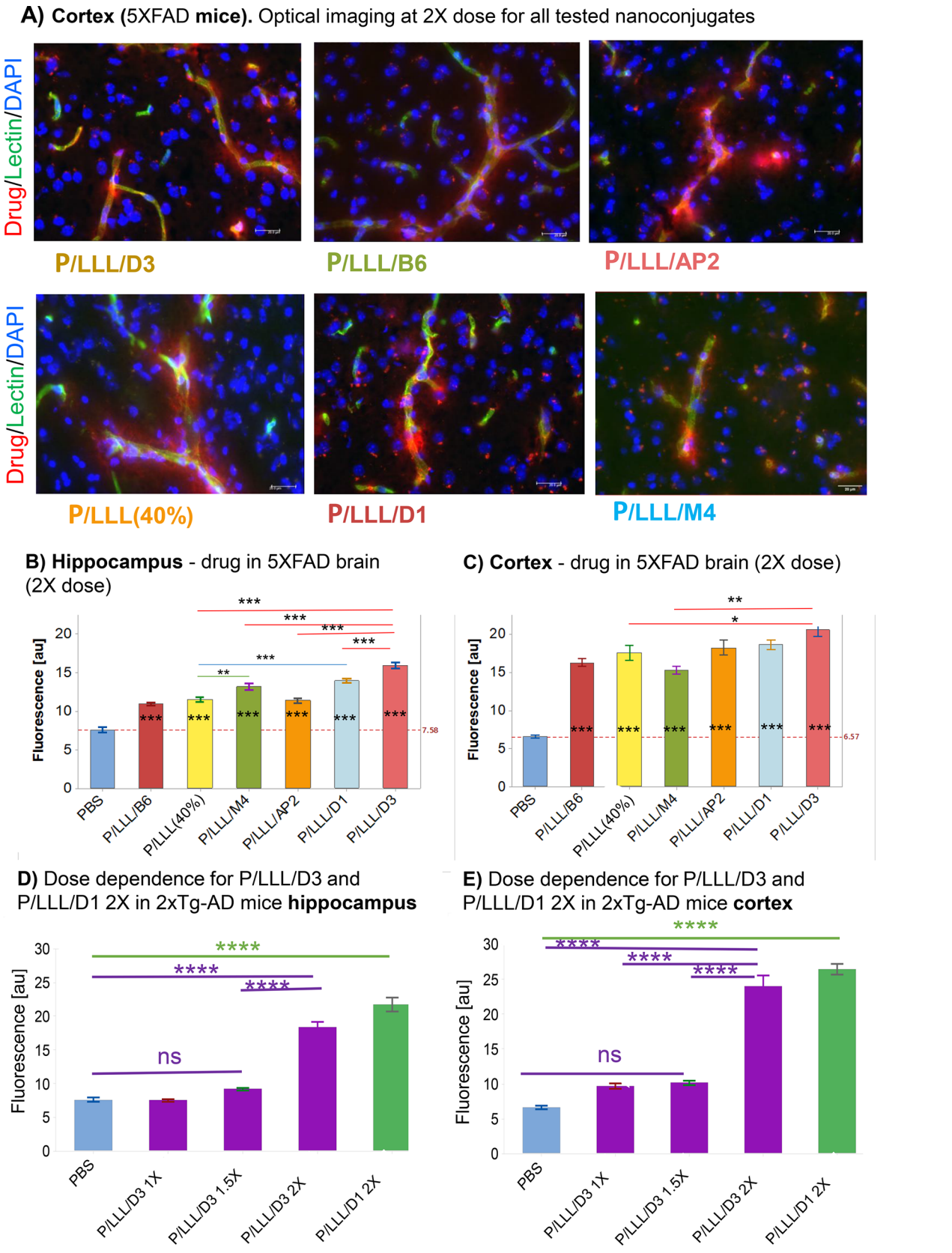

Figure 5. BBB-permeation in AD mouse models. (A) Cortex of 5XFAD mouse at dose 2X. Microscopic visualization of nanoconjugates entering parenchyma from capillary in ADtg after permeating the BBB. Optical imaging of rhodamine-labeled nanoconjugates emerging as a red diffuse halo 120 min after IV-injection into the tail vein. Capillaries are shown in green, nuclei in blue. (B) Hippocampus CA1−3 cell layers and (C) Layers II/III of the somatosensory cortex of 5XFAD-mice, dose 2X of various vectorized nanoconjugates, and P/LLL(40%). Bar graphs indicating permeability efficacies in terms of fluorescence intensity averages from 20 randomly sampled ROI samples away from vasculature (n = 3, 3−4 images per brain region, for each measurement), intensities of PBS-controls not subtracted; nanoconjugates: B6:

https://doi.org/10.1021/acsnano.1c10034
ACS Nano 2022, 16, 11815−11832

Figure 5. continued

hippocampus = t-3.03 p-0.039, cortex t-6.22 p-0.000; M4: hippocampus t-5.08 p-0.000, cortex t-5.62 p-0.00; AP2: hippocampus t-3.44 p-0.011, cortex t-7.51 p-0.000; LLL(40%): hippocampus t-3.56 p-0.007, cortex t-7.06 p-0.000); D3: hippocampus t-10.91 p-0.000, cortex t-11.34 p-0.000; D1: hippocampus t-8.31 p-0.000, cortex t-9.77, p-0.000). All statistical tests were conducted as a one-way ANOVA with Tukey *t* tests (t) comparing nanoconjugate permeability in each brain region. Statistical significance (p) is indicated as * = $p < 0.01$, ** = $p < 0.001$, *** = $p < 0.0001$, and **** = $p < 0.00001$. Error bars represent SEM.

by the known downregulation of LRP-1 expression, but important details remain unsolved such as the pop-up to high permeation activities by the injection of dose 2X P/LLL/D3 conjugate (Figure 5D,E). Could the phenomenon be secondary to additional structural and/or physiological changes during the development of the 2XTg-AD mouse model? These could be (1) the known vascular amyloidosis in ADtg mice, and the flux of Aβ-peptides across the BBB; (2) the downregulation of LRP-1-receptors and their complexation with Aβ-peptides in the AD mice but not in normal brain;[85] (3) structural changes in AD brain capillaries, including increased thickness, splitting and duplication of the basement membrane, altered tight junction morphology, alterations in mitochondria activity, pericytes loss and platelet-derived growth factor receptor beta (PDGFRβ) deficiency, altered perivascular astrocytic processes;[86,87] (4) increase in number and distribution of transporters, such as RAGE, glucose transporter 1 (GLUT-1), and LAT-1, which could increase peripheral concentrations Aβ and other LRP-1 affine-ligands.[88] It is hypothesized that their increased activity could have inactivated LRP-1 by generating high concenrations of affine-ligands, which outcompeted the AP2- and D3-nanoconjugates in Figure 5.

Information on expression of transporters and regulators involved in brain Aβ import/export was obtained by RNA-*Seq* analysis of probes from 3XTg-AD mice brains during their AD-maturation period between age 5 months and 8 months (Figure 6), when producing both Aβ plaques and neuro-fibrillary tangles and several pathological features which resemble human AD. The data in the figure confirmed the FC 1.72-fold (p = 0.000618) upregulation of RAGE (also called Ager; FC = fold-change), insulin receptor-related protein (Insrr) FC 1.79-fold (p = 0.001427), epidermal growth factor (EGF) FC 1.69-fold (p = 0.000483), tight junction proteins claudins (Cldn15) FC 2.03 (p = 0.02086) and (Cldn20) FC = 1.747 (p = 0.03956). Cldn 15 is a cation-selective classical pore forming protein.[89,90] In the intestine, the loss of Cldn15 causes Na^+ deficiency and glucose malabsorption.[91] Cldns 18 and 24 are first expressed in 8-month-old ADtg mice brains. Cldn 18 plays a role in TJ-specific obliteration of the intercellular space, through calcium-independent cell-adhesion activity.[92] On the other hand, Cldns 4 to 9 and Cldn 14 are downregulated in the brains of 8-month-old ADtg mice in comparison with the 5-month-old mice. According to data from network analysis, Cldns 4, 6, and 9 could be involved in BBB and immune cell transmigration via cell adhesion signaling by vascular VCAM-1)/CD106.[93,94] LAT-1 (SLC7a5) is not downregulated, even though many members of the solute SLC-family are dysregulated. RAGE is connected by network analysis data, which provide "relationships" such as physical interactions between protein−orogenetic interactions and which carry specific combinations of mutations[95] relating them to dysregulated Cldns and indirectly to epidermal growth factor EGF and to Insrr (Figure 6B). Dysregulation of RAGE has been shown to increase transfer of Aβ from the blood to the brain by opening tight junctions.[29] Other abnormalities in AD provoke additional brain influx of Aβ peptides while decreasing the levels in the cerebrospinal fluid (CSF) of AD patients.[96−98] RNA-seq analysis revealed no significant increase or decrease of TfR and LRP-1 gene expression during the aging. However, it is not excluded that a decrease in LRP1 expression in the microvasculature was compensated by increased expression in glial cells.[26] In AD, dysregulated LRP-1 and LAT-1 together with other cases of dysregulations contribute to disease promoting the increase of brain Aβ levels via unbalanced influx and efflux.

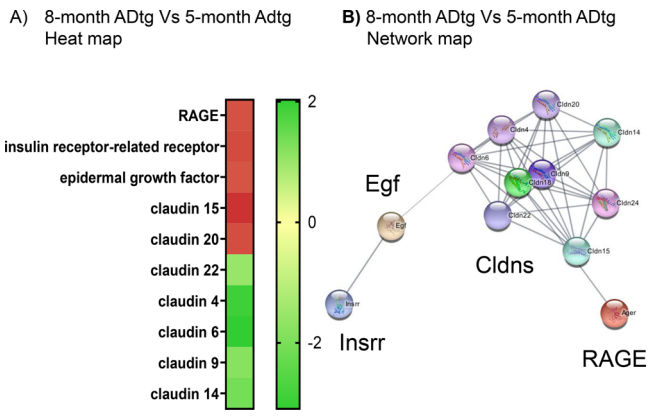

Figure 6. BBB gene expression change during AD progression in a mouse model. (A) Fold-change heat map of gene expression in brains of 8-month-old 3XTg ADtg mice in comparison to 5-month-old 3XTg ADtg mice (red indicates upregulated gene expression; green, downregulated). (B) Network of genes changed in the brains of 8-month-old 3XTg ADtg mice when compared to 5-month-old 3XTg ADtg mice.

Due to inhibition of LRP-1 activity by increased Aβ levels, the endothelial blood-to-brain LRP-1 transcytosis activity of AP2- and D-peptide nanoconjugates (Table 1) is decreased when injected at low nanoconjugate doses (Figure 5). The amelioration seen at high levels of the D-vector-conjugates is consistent with their role as scavenger of Aβ.[52−55] Accordingly, Aβ scavenging restores activity of LRP-1. An overview of the suggested mechanism is illustrated in Figure 7A−C.

Organ Distribution of Nanoconjugate Delivery in AD-Tg Mice and Tumor Mice. The organ distribution of P/LLL/AP2 in normal mice has been previously measured in the organ extracts of normal mice, which had been sacrificed 120 min after tail vein injection of the rhodamine-labeled vector conjugate.[40] P/LLL/AP2/rh accumulated primarily in the kidney and liver, and nanoconjugate fluorescence in the brain was considerably less than in either of these organs.[39] We now added measurements of whole organs and extracts for P/LLL/AP2 in tumor mice, P/LLL/D3 in 5XFAD mice, and P/LLL/D1 and P/LLL/D3 in 2XTg-AD mice in Figure S7A,B. Representative images of P/LLL/AP2 in tumor mice and P/

https://doi.org/10.1021/acsnano.1c10034
ACS Nano 2022, 16, 11815−11832

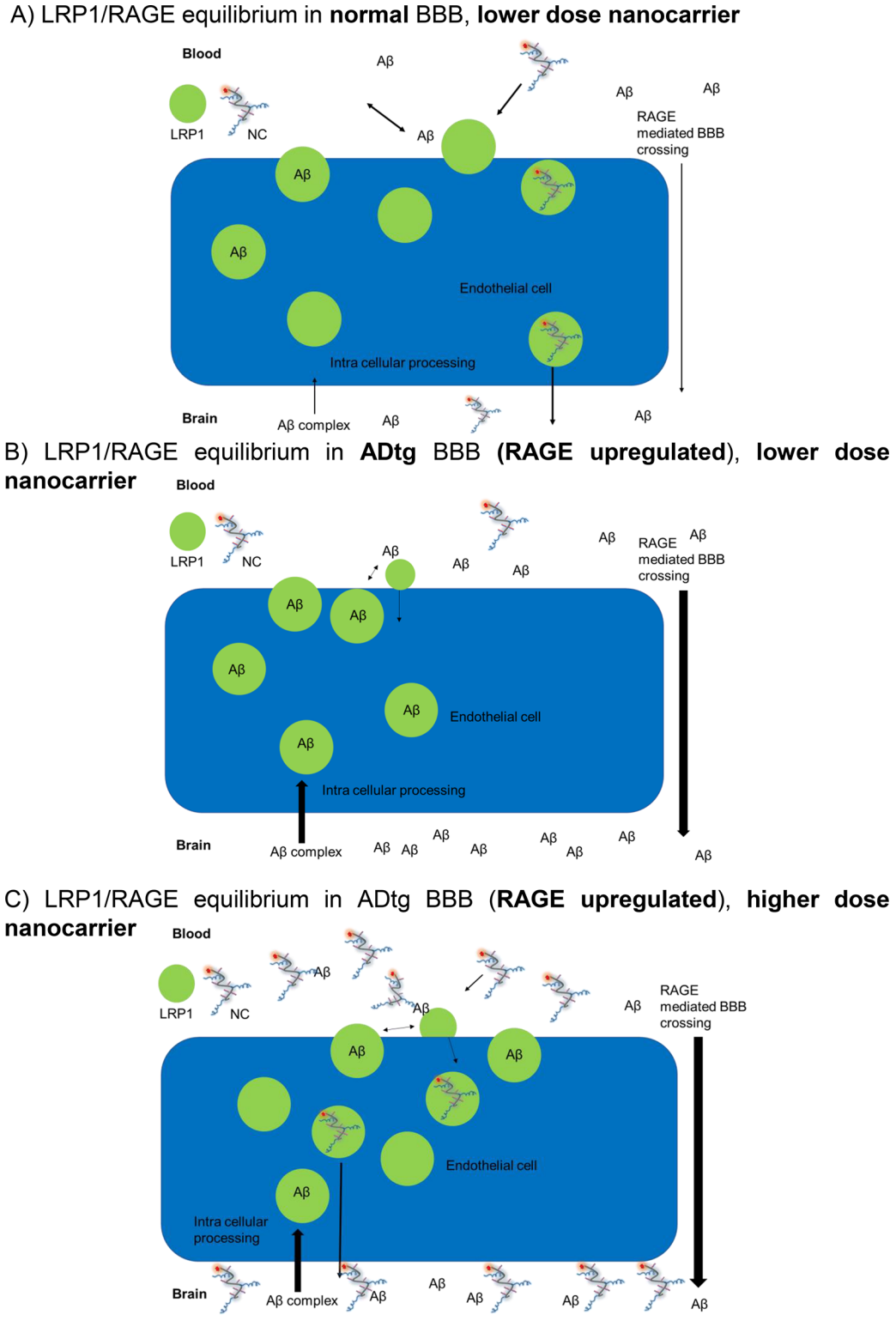

Figure 7. RAGE-dysregulated A*β* accumulation in AD-brain as a mechanism modulating the BBB-permeation of D-vector conjugates. (A) In the normal brain, A*β* does not measurably interfere with D1- or D3-vector-dependent BBB-permeation. Influx and efflux of A*β* are stable, and LRP1 is available to facilitate nanoconjugate transcytosis even at low doses. (B) In the brains of 5XFAD-mice, A*β* levels are high in part due to upregulated influx activity of RAGE. A*β* binds to a large fraction of D-vectors and leaves only a small fraction available for transcytosis. In addition, A*β* binds to LRP1 and inhibits transcytosis through endothelial layer for BBB-permeation. (C) However, at an elevated dose of 2X, a significant, sharp increase in nanoconjugate permeation is seen (Figure 5D,E). We hypothesize that in this case, inhibition by A*β* is overcome now by amyloid scavenging through added surplus 2X D-vector-conjugate which now also assists refurbishing LRP1 to become available for transcytosis.

LLL/D1 in 2XTg-AD mice are shown in Figure S7A. Quantification of the organs in Figure S7B revealed high fluorescence intensity for tumor in the case of P/LLL/AP2 accounting for 32% of the total in heart, kidneys, spleen, liver,

https://doi.org/10.1021/acsnano.1c10034
ACS Nano 2022, 16, 11815−11832

lungs, and brain (Figure S7B-I). In 5XFAD mice, the fluorescence of P/LLL/D3 in the brain accounted for 5.1%, while the major uptake was seen in the kidneys and to a lesser extent in the liver (Figure S7B-II). A similar distribution was seen in 2XTg-AD mice. P/LLL/D3 uptake in the brain was 4.5% of the organs in Figure S7B-III, while P/LLL/D1 uptake in the brain was 4.25% in Figure S7B-IV.

Signatures of BBB Pathways in Normal, AD, and Tumor Brain. A summary of signatures for BBB-permeation in normal, brain tumor, and AD brains is illustrated in Figure 8.

A) Fluorescence intensity (permeation) in cortex of normal and 5XFAD mice at a dose of **2X**

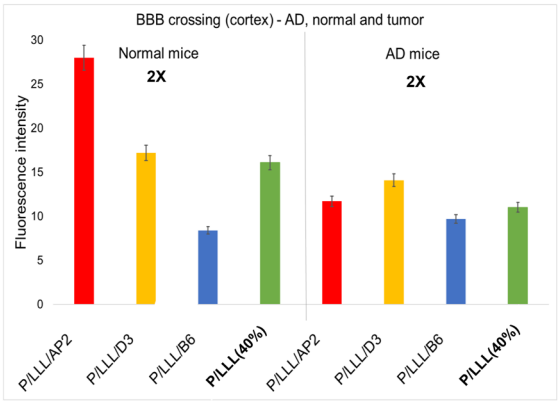

B) Comparison of fluorescence intensity, cortex of normal brain (2X dose) and glioblastoma (1X dose) – means after PBS subtraction

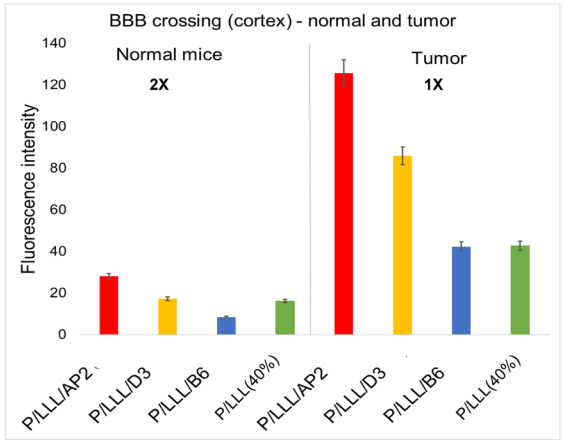

Figure 8. Comparison of downregulated nanoconjugate permeation in ADtg-brain with upregulated nanoconjugate permeation in tumor and with low BBB permeation in normal mice. (A) BBB-permeation efficacies (in terms of fluorescence intensity) in cortex of ADtg-brain (5XFAD) at dose 2X is significantly reduced in comparison with the cortex of the normal brain (BL/6 mice) for P/LLL/AP2, P/LLL/D3, P/LLL/B6, and P/LLL(40%). (B) Comparison of normal mice at a dose of 2X with tumor-bearing mice at dose of 1X. Error bars represent SEM.

The efficacy at dose 2X is depicted for 5XFAD ADtg mice and normal mice in Figure 8A. The efficacy for normal mice at dose 2X is displayed together with that of tumor-bearing mice at the lower dose 1X in Figure 8B. By comparing details in the chemical structure of P/LLL nanoconjugates and their BBB-permeation efficacy *in vivo*, we propose general and specific (signature) criteria in normal brain, ADtg brain, and tumor-bearing brains. (1) The normal mouse brain serves as the prototype BBB and the diseased brains as the abnormal variants. The description of the LRP1- and TfR-pathways may serve as an example of the receptor system located at the apical and contralateral membrane surface of brain vascular endothelia.[99−102] The active carriers consist of the amphiphilic platform P/LLL(40%) and the vectors AP2, D1, D3, M4, or B6. The amphiphilic nanoconjugates bind to the membrane surface at preferred sites before transcytosis. We hypothesize that P/LLL(40%) attaches to membranes of endothelial cells, which also expose the transcytosis receptors LRP1 and TfR. After allosterically induced exposure of the receptor sites, the specific vectors are complexed with high affinity, and specific transcytosis is initiated. An example for membrane surface binding has been reported for P/LLL(40%) before inducing liposome leakage.[42,43] Similarly, polymersomes have been shown to attach to endothelial surface before binding to LRP1.[103,104] (2) The induced allosteric change provides both a sterically improved juxta-positioning and a high affinity for the formation of the vector−receptor complex. The observed supra-linear dose dependence suggests that dose-dependent occupation of LLL sites contributes a steric and energetic basis for the vector−receptor permeation through the BBB. (3) In ADtg-mice, RAGE receptor is upregulated, leading to increased levels of Aβ which engage in complex formation with LRP1 and inhibit the transcytosis of AP2-, D1-, and D3-nanoconjugates. At a higher dose (~2X) of D3 or D1, inhibition was ameliorated as the concentration of the nanoconjugates surpasses the level of free and LRP1-bound Aβ. Scavenging by Aβ-vector complexation and dissociation of Aβ-LRP1 to yield free LRP1 gave rise to the abrupt increase in the BBB permeation efficacy, which was observed for the D-nanoconjugates.

Signatures by Ranking of P/LLL(40%)−Vector Conjugates. Normal and diseased brain including dysregulated amyloid levels may afford distinct reactions with transcytosis-active nanoconjugates to provide successful BBB delivery including vector Aβ-scavenging. This may give rise to a ranking in the performance of successful delivery (Table S4). The hierarchy for the tumor in BL/6 mice at dose 1X indicates that AP2-nanoconjugates have the highest permeability, also in agreement with the efficacy displayed in the contralateral hemisphere of tumor-bearing mice (Tables S3, S4, S5). The efficacy ranking is similar for normal BL/6 mice at dose 2X and also in the hierarchy for normal Balb/c mice[40] at dose 1X (Table S4). In contrast with the agreement at different doses 1X and 2X, the top position at dose 1X for normal BL/6 mice is given to D1-conjugate (Table S4). The finding could suggest that the hierarchy in the brain of the BL/6-tumor mouse at dose 1X is similar to the hierarchy in normal Balb/c mice at dose 1X. Because of vector-Aβ scavenging, the top positions in the hierarchy for 5XFAD at dose 2X is shared between conjugates of D3, D1, and AP2 (Table S4). In conclusion, the hierarchy positions for AP2, D1, and D3 do not vary significantly whether the brain is normal, tumor containing, or AD-brain. A similar conclusion is obtained when considering the positions of vector conjugates for M4 and B6 following in positions after AP2, D1, and D3. Regarding minor efficacy variations, ranking in the AD brain, the dominant position is given to AP2 at low levels of conjugates; however, it is given to D1 and D3 at dose 2X, which is significant in the hippocampus, the epicenter of AD pathology. The lack of LRP1-availability in the presence of high Aβ levels should guide the choice of applied delivery vehicle.

https://doi.org/10.1021/acsnano.1c10034
ACS Nano 2022, 16, 11815−11832

CONCLUSIONS

We have presented an extensive study of the ability of nanoconjugates to cross the BBB *in vitro* and *in vivo* in mouse models of normal (healthy) brains, AD-like brains, and tumor-bearing brains. We employed a optical fluorescence microscope analysis method to understand molecular mechanisms that regulate cross talks between transcytosis pathways and efficacy of BBB crossing, *in vitro* Transwell tests to identify route-sharing by competition, factorial analysis to elucidate the interplay of vectors when colocated on the same carrier molecule, RNA-*Seq* analysis to strengthen the idea that temporal gene expression can steer variants in ADtg mouse models, and the awareness that dysregulated receptors because of their cross-talks could be powerful game changers.

The results obtained for a multireactive site nanoconjugate are highly significant in guiding the design of drug delivery to the brain parenchyma. We have extensively characterized and compared different vector-conjugates transported in different BBB transcytosis pathways and their receptor-, dose-, and location-dependent endothelial permeation efficacy. Based on the results for brain in normal, AD models. and brain tumor of mice, signature patterns were derived that distinguish vector conjugates and different brain status. Qualitatively reproducible hierarchy arrays of shuttle peptide efficacy followed dose-dependent patterns reflecting different brain status location efficacies. The arrays can be useful as sensitive indicators of receptors, permeation pathways, disease-dependent endothelial structure, location, and indicators linking efficacy and brain health status. In these regards, the signature data reflected mechanisms of vector recognition by transcytosis receptors, the influence of endothelial membrane binding, competition of Aβ amyloid peptides, and the amphiphilic nature of the nanopolymer portion of the vector conjugates.

In vitro BBB (Transwell) studies confirmed that P/LLL nanoconjugates were contained during the experiment in all endothelial cells consistent with the passage of the vectors through the cells and not through paracellular tight junctions. *In vitro* competition assays also indicated the involvement of LAT-1 in the BBB-transfer mechanisms of D3 and AP2 peptides, and their competition with Aβ. Factorial analysis of tumor brain tissue confirmed coupling between coligated AP2 and B6 vectors to enhance tumor selectivity. Coupling is also indicated by our findings of supra-linear dose dependency for normal brain,[39] AD-like brain, and tumor-bearing brains. Evidently, factorial analysis can give consistent results when applied to brain with different health status and in different brain locations, and coupling reflects variation in vector loading and dose dependence.

Normal brain status and different pathologies call for different strategies regarding nanoconjugate composition and systemic dosage. These findings may lead to a better and more efficient design of nanomaterials aimed at the delivery of therapeutic cargo to CNS targets under normal and pathological conditions.

EXPERIMENTAL SECTION – MATERIALS AND METHODS

Materials. Highly purified poly(β-L-malic acid) was prepared from the culture broth of *Physarum polycephalum* as described.[40] Custom-made peptides Angiopep-2 (AP2) (TFFYGGSRGKRNNFKTEEYC-NH_2), D1 (qshyrhispaqvc), D3 (rprtrlhthrnrc), and ACI89 (pshyrh-ispaqkc) all with an additional cysteine group, Miniap-4 (H-[Dap]KAPETALD-NH_2, with external lactam-ring) and TfR-ligand B6 (CGHKAKGPRK) were purchased from AnaSpec Inc. (Fremont, CA, USA). The D-configured peptides are mirror-copies of L-peptides identified previously via phage-display in α-D-amino acid configurations. Rhodamine-C2 was purchased from Fisher Scientific (Hampton, NH, USA). Maleimide-PEG(3400)-maleimide and maleimide-PEG(2000)-SCM were purchased from JenKem Technology (Plano, TX, USA). DyLight488 tomato-lectin (DL-1174) was purchased from Vector Laboratories, Burlingame, CA. Tri-Leucine was ordered from Bachem Inc. (Torrance, CA, USA), while Aβ_{1-40}, DCC, NHS, TFA, MEA, and DTT were purchased from Sigma-Aldrich (St. Louis, MO, USA). Sephadex G-75 resin and PD-10 columns were purchased from GE Healthcare (Chicago, IL, USA). Vivaspin centrifuge filter tubes were purchased from Sartorius (Stonehouse, UK). PMLA/LLL(40%)/MEA(10%) ("PMLA *pre*-conjugate"), peptide-PEG3400-maleimide, and peptide-PEG2000-maleimide were synthesized as described pereviously.[40] For Transwell competition assays, JPH203 ($C_{23}H_{19}Cl_2N_3O_4$; purity >98% by NMR, ChemScene, NJ, USA) was dissolved in DMSO to 10 mM and diluted to 10 μM in cell differentiation medium. Human Aβ_{1-40} (>90% by HPLC; Sigma-Aldrich) was dissolved in calcium-free and magnesium-free sterile DPBS to form a stock solution of 1 mg/mL. hCMEC/D3 (Human Cerebral Microvascular Endothelial Cells, Clone D3) were purchased from Cedar Lane Laboratories (NC, USA, catalog # CLU512). PMLA-vector conjugates were nontoxic to mice and *Cynomolgus macaques* chimpanzee.

General Synthesis of PMLA/LLL(40%)/Peptide(2%)/Rhodamine(1%).[40] Four milligrams (15 μmol) of preconjugate monomer, PMLA/LLL(40%)/MEA(10%)[40] (260 g/mol) were dissolved in 800 μL of phosphate buffer pH 6.3 and placed in a glass vial with a magnetic stirrer at ambient temperature. In order to achieve 2% loading, 1.78 mg of Angiopep-2-PEG3400-maleimide (5803 g/mol), 1.68 mg of ACI89-PEG3400-maleimide (4923g/mol), 1.58 mg D3-PEG3400-maleimide (5103 g/mol), 1.67 mg D1-PEG3400-maleimide (4925 g/mol), 1.33 mg of B6-PEG3400-maleimide (4480 g/mol), or 0.86 mg M4-PEG2000-maleimide (2796 g/mol) were dissolved in phosphate buffer pH 6.3 to a concentration of 10 mg/mL and were added dropwise to the reaction mixture. After 1 h, reactions were completed as monitored using SEC-HPLC (220 nm wavelength). Rhodamine-maleimide (0.104 mg for 1% loading, 680.79 g/mol, 0.149 μmol, 52 μL of 2 mg/mL solution in DMF) was loaded forming thioethers with the PMLA platform at pendant MEA-SH. The reaction was conducted in the dark and was monitored using SEC-HPLC. The number of loaded dye molecules was determined via rhodamine absorbance in the PMLA conjugate elution peak. After stirring for a further 1−2 h, 10 mg of N-ethylmaleimide in 50 μL of DMF were added to cap the free SH groups. Nanoconjugates were purified over a PD-10 column using distilled water lyophilized and stored at −20 °C. In the following, chemical formulas were simplified by omitting the symbols representing rhodamine and percent loadings.

Details on materials and on biological methods are presented at the end of the article and in Supporting Information. Nanoconjugate characterization[40] including chemical nomenclature, SEC-HPLC retention times, calculated molecular weight, and ζ potential is listed in Table S1. The negative ζ potential of the nanoconjugates ranging from −5.5 to −11.6 mV were in the range suitable for crossing BBB.[39] The hydrodynamic diameters were consistently below 7 nm as previously published.[39]

***In Vitro* (Transwell) BBB Permeability of Vectors.** Concentration of nanoconjugates in the apical compartment was 4.55 μM, corresponding to 0.7 μM in the blood of mice injected in dose 0.125X (see definition in Table S2). Apical concentrations of the inhibitors were 10 μM of JPH203, 10 μM of AP2, and 0.219 ng/mL of Aβ peptide (mimicking the peptide levels in healthy blood).[39] The basolateral concentration of Aβ peptide was 9.8 ng/mL.[39] Samples were taken at multiple time points until 3 h from the addition of nanoconjugates, and fluorescence was measured to calculate endothelial permeability. The permeation of P/LLL/D3, P/LLL/AP2, and P/LLL(40%) through the human brain microvascular endothelial cell monolayer was tested in the presence of the inhibitors.

https://doi.org/10.1021/acsnano.1c10034
ACS Nano 2022, 16, 11815−11832

Analysis confirmed that TJ proteins remained intact, as indicated by the maintenance of *trans*-endothelial electric resistance (TEER) (Supporting Information Figure S3). The MTS assay at nanoconjugate concentrations of 9.1, 18.2, and 36.4 μM (6.7-fold above the blood levels after *in vivo* injection of doses 0.25X, 0.5X, and 1X in Table S2) showed that none of the nanoconjugates significantly decreased cell viability in the presence of the *in vivo* equivalent of 1X dosage.

Mouse *In Vivo* BBB Permeability of Vector Nanoconjugates. We tested the P/LLL(40%) nanoconjugates of vectors D1, D3, and ACI-89. Healthy mice C57BL/6J (BL/6), AD-mouse models, or a Glioma mouse model were tested. After IV injection of 1X dose of conjugates (dose as defined in Table S2), mice were euthanized 120 min post injection. Under the morphological analyses, brain slices displayed at variable times the red fluorescence of the vector conjugates appearing around microvasculature at distinct locations in the brain parenchyma (Figure 1A). After color conversion into gray scale, which improved the sensitivity and accuracy of regions of interest, fluorescence intensities were measured (ROIs, Figure 1A, yellow rectangles), thereby carefully excluding damaged vascular and pre-existing colored particulates known as lipofuscin, a waste deposit in neurons.[105−107,]

Animal Procedures. Details for hosting normal mice, AD mouse models, glioblastoma mouse models are presented in Supporting Information.

Intravenous Animal Injections. Nanoconjugates were injected into tail veins of 11-week-old C57BL/6J (BL/6)-mice with intracranial glioblastoma, cell line GL261. Injections followed the details described above for normal mice and ADtg-mice. After injection, mice were promptly returned to their cages. At fixed times 15 min before euthanasia, mice were injected with a mix of 75 μL Tomato Lectin (DyLight 488 *Lycopersicon esculentum* (Tomato) Lectin, catalog # DL-1174 Vector laboratories, 1 mg/mL) and 50 μL Ricin Lectin (Fluorescein *Ricinus communis* Agglutinin I (RCA 120), catalog # FL-1081 Vector laboratories, 5 mg/mL) to label vessels in tumor and brain. Mice were then anesthetized and euthanized by cervical dislocation followed by decapitation at 2 h or any selected time after the injection of nanoconjugates. Brains were collected, saved in OCT, and used for optical analysis.

Image Acquisition and Optical Analysis. Imaging and optical analysis were performed with a Lecia DM 6000B epifluorescence microscope (Leica Microsystems, Wetzlar, Germany). Rhodamine-labeled nanoconjugates were visualized with a 534−558 nm excitation and 560−640 nm emission filter set, viewed with a 20X Leica HC Plan Apo 0.70 N.A. and a 40X Leica HCX Plan Apo 0.85 N.A. lens, and recorded with a Leica DFC 360 FX camera. The camera was controlled with Leica LAS X software, and images were acquired with 4.0 s + 2.0 gain exposures with the 20X and 40X lenses. These parameters were held constant to enable image-to-image comparisons across specimens.

Optical imaging data analysis was performed with ImageJ FIJI software. To determine if our nanoconjugates entered the brain parenchyma, we performed an image intensity analysis in regions apart from vasculature (see yellow boxes in Figure 1A). In this analysis, 10 × 10 mm^2 sized regions of interest (ROI) were randomly overlaid on images showing the vasculature, avoiding blood vessels, to avoid bias in data collection. Our statistical analysis rests on at least n = 3 animals for each group of experiments, at least n = 3 images from each brain section, and at least 20 ROI were measured on each image, which provides 180 readings per brain region. Overall levels of nanoconjugate labeling are shown as means and standard error of the mean for 20 measurements from separate images of the hippocampal CA1−3 layers, layers II/III of the somatosensory or visual cortices, and the superior and inferior midbrain colliculi in normal and ADtg mice. Data plots and statistical analysis were conducted in Prism or in Minitab. Unless indicated otherwise, fluorescence measurements were compared via one-way ANOVA combined with pairwise *post-hoc* comparisons of individual data points; exact parameters and tests are indicated for each result. Statistical significance is indicated as follows: * = $p < 0.01$, ** = $p < 0.001$, and *** = $p < 0.0001$.

Organ Biodistribution of PMLA-Vectors by Fluorescence Imaging of Organs at 120 min post IV Injection. Fluorescence of major organs brain, heart, kidney, and organs of RES (liver, spleen, and lung) was measured at 120 min after IV injection of fluorescence-labeled agents. The analysis was performed using an IVIS Lumina XR Optical Imaging System (PerkinElmer, Richmond, CA, USA) using DsRed filter sets.[39] Organ and brain fluorescence were simultaneously measured in all tissue samples from each experiment to attain consistent imaging parameters. Imaging and comparison of whole organs refer to authentic mice.

Factorial Study Analysis. The multivariable BBB permeation study of P/LLL/AP2 in tumor-bearing brains (Case 1. Single vector), in comparison with P/LLL/AP2/B6 at varied dosage (Case 2. Coligated vectors AP2 and B6 tested in tumor and normal brain of the same animal) was studied by Factorial Study Analysis.[77−79] Fluorescence-labeled permeation into the tumor (response T), into the nontumor brain (NT), and the tumor selectivity (response T/NT) were the measured parameters. (For DoE, Design of Experiment, see Supporting Information). For Table 2 and Figure 4 see main text. For Table S3 and Figure S5, see Supporting Information.

The experimental DoE-matrices containing factors were "the vector peptide AP2 loading", "Dose X", and the response "Fluorescence Intensity" for both tumor and nontumor brain and the tumor "Selectivity". The AP2-matrix for experiments with P/LLL/AP2 and the combined matrix for experiments with p/LLL/AP2/B6, which loaded both the vector AP2 of the LRP-1 transcytosis and B6 of the TfR-transcytosis pathway, can be seen in Table 2. Each matrix also contained a "center-point": in the AP2-matrix, fluorescence intensity and selectivity were given for P/LLL/AP2(1%) at a dose of 0.625X (Table 2A). In the combined matrix, responses were measured for P/LLL/B6(1%)/AP2(1%) at the dose 0.625X (Table 2B). The DoE software generated several plots: a "contour"-plot (Figure 4), a "significance"-plot ("Pareto chart of the Standardized Effects", Figures S6B1,B2), and an "interaction"-plot (Figures S6C1,C2). In the contour plots (Figure 4), values of selectivity (T/NB see also Table S3) is coded in different shades of blue.

RNA-*Seq* Analysis. Brains of triple transgenic (3xTg, Tg-(APPSwe,tauP301L)1Lfa), Jackson laboratories) AD mice (5 were compared at 5 months old and 8 months old. Brains were rapidly removed following euthanasia at defined ages. Total RNA was extracted from mouse brains via TRIzol extraction (Invitrogen, Carlsbad, CA). The concentration of RNA was determined by NanoDrop ND-1000 Spectrophotometer (NanoDrop Technologies, Wilmington, DE) using 260/280 nm ratios (≥1.8) to assess sample purity. Total RNA integrity was determined with the Agilent 2100 Bioanalyzer system (Agilent Technologies, Palo Alto, CA) and only samples with an RNA integrity number (RIN) ≥ 8 were used for RNA-*Seq*. RNA-*Seq* was completed at the UCLA Technology Center for Genomics & Bioinformatics. Libraries for RNA-*Seq* were prepared with a KAPA Stranded RNA-*Seq* Kit. The workflow consists of mRNA enrichment, cDNA generation, and end repair to generate blunt ends, A-tailing, adaptor ligation, and PCR amplification. Different adaptors were used for multiplexing samples in one lane. Sequencing was performed on Illumina Hiseq3000 for a single 50 run read. Data quality check was done on Illumina SAV. Demultiplexing was performed with the Illumina Bcl2fastq2 v 2.17 program. The reads were first mapped to the latest UCSC transcript set using Bowtie2 version 2.1.0, and the gene expression level was estimated using RSEM v1.2.15. Quality control of data was done using MultiQC v1.4.

Network retrieval was done using Cytoscape 3.8 software, using the STRING database for *Mus muculus*. Heat maps were generated using Prism. Statistical analysis was carried out pairwise with multiple *t* tests, two-stage linear step-up procedure of Benjamini, Krieger, and Yekutieli.

ASSOCIATED CONTENT

Supporting Information

The Supporting Information is available free of charge at https://pubs.acs.org/doi/10.1021/acsnano.1c10034.

https://doi.org/10.1021/acsnano.1c10034
ACS Nano 2022, 16, 11815−11832

Details of materials and methods section with procedures for chemistry, *in vitro* and *in vivo* procedures such as Transwell permeation and competition experiments, optical imaging of organs after injection for biodistribution, factorial analysis, nomenclature, structure, and physical properties of nano conjugates, including tables and figures (PDF)

AUTHOR INFORMATION

Corresponding Authors

Julia Y. Ljubimova − *Terasaki Institute for Biomedical Innovation (TIBI), Los Angeles, California 90024, United States*; Email: ljubimova1@gmail.com

Eggehard Holler − *Terasaki Institute for Biomedical Innovation (TIBI), Los Angeles, California 90024, United States*; orcid.org/0000-0001-8582-2190; Email: eholler@terasaki.org

Authors

Liron L. Israel − *Department of Neurosurgery, Cedars-Sinai Medical Center, Los Angeles, California 90048, United States*; orcid.org/0000-0003-4411-5857

Anna Galstyan − *Department of Neurosurgery, Cedars-Sinai Medical Center, Los Angeles, California 90048, United States*

Alysia Cox − *Department of Neurosurgery, Cedars-Sinai Medical Center, Los Angeles, California 90048, United States*

Ekaterina S. Shatalova − *Department of Neurosurgery, Cedars-Sinai Medical Center, Los Angeles, California 90048, United States*

Tao Sun − *Department of Neurosurgery, Cedars-Sinai Medical Center, Los Angeles, California 90048, United States*

Mohammad-Harun Rashid − *Department of Neurosurgery, Cedars-Sinai Medical Center, Los Angeles, California 90048, United States*

Zachary Grodzinski − *Department of Neurosurgery, Cedars-Sinai Medical Center, Los Angeles, California 90048, United States*

Antonella Chiechi − *Department of Neurosurgery, Cedars-Sinai Medical Center, Los Angeles, California 90048, United States*

Dieu-Trang Fuchs − *Department of Neurosurgery, Cedars-Sinai Medical Center, Los Angeles, California 90048, United States*

Rameshwar Patil − *Department of Neurosurgery, Cedars-Sinai Medical Center, Los Angeles, California 90048, United States*

Maya Koronyo-Hamaoui − *Department of Neurosurgery and Department of Biomedical Sciences, Division of Applied Cell Biology and Physiology, Cedars-Sinai Medical Center, Los Angeles, California 90048, United States*

Keith L. Black − *Department of Neurosurgery, Cedars-Sinai Medical Center, Los Angeles, California 90048, United States*

Complete contact information is available at: https://pubs.acs.org/10.1021/acsnano.1c10034

Author Contributions

#Lead experimental contributor

Notes

Mouse maintenance and experimental procedures followed the guidelines established by the Cedars Sinai Institutional Animal Care and Use Committee (IACUC).

The authors declare no competing financial interest.

ACKNOWLEDGMENTS

This work was supported by the Department of Neurosurgery, CSMC and Health Effects of Air Pollution Foundation Agreement No. BTAP011, BTAP013 and HEAPF015 (KLB) by NIH R01 Grants CA188743, CA 206220 (JYL), CA 209921 (EH). We also want to thank Michael T. Kleinman (UC Irvine) for his help in maintaining the 3xTg ADtg mice.

REFERENCES

(1) Siegal, T.; Zylber-Katz, E. Strategies for Increasing Drug Delivery to the Brain. *Clinical pharmacokinetics* **2002**, *41* (3), 171−186.

(2) Siegal, T.; Horowitz, A.; Gabizon, A. Doxorubicin Encapsulated in Sterically Stabilized Liposomes for the Treatment of a Brain Tumor Model: Biodistribution and Therapeutic Efficacy. *Journal of neurosurgery* **1995**, *83* (6), 1029−1037.

(3) Dong, X. Current Strategies for Brain Drug Delivery. *Theranostics* **2018**, *8* (6), 1481−1493.

(4) Webster, D. M.; Sundaram, P.; Byrne, M. E. Injectable nNanomaterials for Drug Delivery: Carriers, Targeting Moieties, and Therapeutics. *Eur. J. Pharm. Biopharm.* **2013**, *84* (1), 1−20.

(5) Wong, H. L.; Wu, X. Y.; Bendayan, R. Nanotechnological Advances for the Delivery of CNS Therapeutics. *Adv. Drug Delivery Rev.* **2012**, *64* (7), 686−700.

(6) Walkey, C. D.; Chan, W. C. W. Understanding and Controlling the Interaction of Nanomaterials with Proteins in a Physiological Environment. *Chem. Soc. Rev.* **2012**, *41*, 2780.

(7) Yu, Y. J.; Zhang, Y.; Kenrick, M.; Hoyte, K.; Luk, W.; Lu, Y.; Atwal, J.; Elliott, J. M.; Prabhu, S.; Watts, R. J. Boosting Brain Uptake of a Therapeutic Antibody by Reducing its Affinity for a Transcytosis Target. *Science translational medicine* **2011**, *3* (84), 84ra44−84ra44.

(8) Zlokovic, B. V. Neurovascular Pathways to Neurodegeneration in Alzheimer's Disease and Other Disorders. *Nature reviews. Neuroscience* **2011**, *12* (12), 723−38.

(9) Zenaro, E.; Piacentino, G.; Constantin, G. The Blood-Brain Barrier in Alzheimer's Disease. *Neurobiology of Disease* **2017**, *107*, 41−56.

(10) Zipser, B.; Johanson, C.; Gonzalez, L.; Berzin, T.; Tavares, R.; Hulette, C.; Vitek, M.; Hovanesian, V.; Stopa, E. Microvascular Injury and Blood−Brain Barrier Leakage in Alzheimer's Disease. *Neurobiology of aging* **2007**, *28* (7), 977−986.

(11) Zuroff, L.; Daley, D.; Black, K. L.; Koronyo-Hamaoui, M. Clearance of Cerebral Aβ in Alzheimer's Disease: Reassessing the Role of Microglia and Monocytes. *Cell. Mol. Life Sci.* **2017**, *74* (12), 2167−2201.

(12) Carare, R. O.; Koronyo-Hamaoui, M.; Hainsworth, A.; Holtzman, D.; Ihara, M.; Jefferson, A.; Kalaria, R. N.; Kipps, C.; Kanninen, K.; Leinonen, V.; McLaurin, J.; Miners, S.; Malm, T.; Nicoll, J. A. R.; Piazza, F.; Paul-Visse, G.; Saito, S.; Shih, A.; Scholtzova, H.; Snyder, H.; Snyder, P.; Zlokovic, B.; et al. Cerebrovascular Disease and the Failure of Elimination of Amyloid-β From the Brain and Retina with Age and Alzheimer's Disease. Opportunities for Therapy. *Alzheimer's Dement (Amst).* **2020**, *12*, No. e12053.

(13) Shi, H.; Koronyo, Y.; Fuchs, D. T.; Sheyn, J.; Wawrowsky, K.; Lahiri, S.; Black, K. L.; Koronyo-Hamaoui, M. Retinal Capillary Degeneration and Blood-Retinal Barrier Disruption in Murine Models of Alzheimer's Disease. *Acta Neuropathol Commun.* **2020**, *8*, 202.

(14) Maeda, H.; Bharate, G. Y.; Daruwalla, J. Polymeric Drugs for Efficient Tumor-Targeted Drug Delivery Based on EPR-Effect. *Eur. J. Pharm. Biopharm.* **2009**, *71* (3), 409−419.

(15) Huynh, E.; Zheng, G. Cancer Nanomedicine: Addressing the Dark Side of the Enhanced Permeability and Retention Effect. *Nanomedicine* **2015**, *10* (13), 1993−1995.

(16) DeSantis, C. E.; Lin, C. C.; Mariotto, A. B.; Siegel, R. L.; Stein, K. D.; Kramer, J. L.; Alteri, R.; Robbins, A. S.; Jemal, A. Cancer Treatment and Survivorship Statistics, 2014. *CA: A cancer journal for clinicians* **2014**, *64* (4), 252−271.

(17) Nichols, J. W.; Bae, Y. H. EPR: Evidence and Fallacy. *J. Controlled Release* **2014**, *190*, 451−464.
(18) Danhier, F. To Exploit the Tumor Microenvironment: Since the EPR Effect Fails in the Clinic, What is the Future of Nanomedicine? *J. Controlled Release* **2016**, *244*, 108−121.
(19) Ramanathan, A.; Nelson, A. R.; Sagare, A. P.; Zlokovic, B. V. Impaired Vascular-Mediated Clearance of Brain Amyloid Beta in Alzheimer's Disease: the Role, Regulation and Restoration of LRP1. *Frontiers in Aging Neuroscience* **2015**, *7*, 136.
(20) Uhlen, M.; Zhang, C.; Lee, S.; Sjöstedt, E.; Fagerberg, L.; Bidkhori, G.; Benfeitas, R.; Arif, M.; Liu, Z.; Edfors, F.; Sanli, K.; von Feilitzen, K.; Oksvold, P.; Lundberg, E.; Hober, S.; Nilsson, P.; Mattsson, J.; Schwenk Jochen, M.; Brunnström, H.; Glimelius, B.; Sjöblom, T.; Edqvist, P.-H.; Djureinovic, D.; Micke, P.; Lindskog, C.; Mardinoglu, A.; Ponten, F. A pathology atlas of the human cancer transcriptome. *Science* **2017**, *357* (6352), 1 DOI: 10.1126/science.aan2507.
(21) The Human Protein Atlas; proteinatlas.org, ver. 21.0; Atlas updated: 2021−11−18, last accessed 2022−5−17.
(22) Grimmer, T.; Goldhardt, O.; Guo, L.-H.; Yousefi, B. H.; Förster, S.; Drzezga, A.; Sorg, C.; Alexopoulos, P.; Förstl, H.; Kurz, A. LRP-1 Polymorphism is Associated with Global and Regional Amyloid Load in Alzheimer's Disease in Humans *in-Vivo*. *NeuroImage: Clinical* **2014**, *4*, 411−416.
(23) Daniels, T. R.; Delgado, T.; Rodriguez, J. A.; Helguera, G.; Penichet, M. L. The Transferrin Receptor Part I: Biology and Targeting with Cytotoxic Antibodies for the Treatment of Cancer. *Clinical Immunology* **2006**, *121* (2), 144−158.
(24) Inoue, S.; Patil, R.; Portilla-Arias, J.; Ding, H.; Konda, B.; Espinoza, A.; Mongayt, D.; Markman, J. L.; Elramsisy, A.; Phillips, H. W.; Black, K. L.; Holler, E.; Ljubimova, J. Y. Nanobiopolymer for Direct Targeting and Inhibition of EGFR Expression in Triple Negative Breast Cancer. *PLoS One* **2012**, *7* (2), No. e31070.
(25) Fabrichny, I. P.; Leone, P.; Sulzenbacher, G.; Comoletti, D.; Miller, M. T.; Taylor, P.; Bourne, Y.; Marchot, P. Structural Analysis of the Synaptic Protein Neuroligin and its β-Neurexin Complex: Determinants for Folding and Cell Adhesion. *Neuron* **2007**, *56* (6), 979−991.
(26) Kanekiyo, T.; Bu, G. The low-Density Lipoprotein Receptor-Related Protein 1 and Amyloid-Beta Clearance in Alzheimer's Disease. *Front Aging Neurosci* **2014**, *6*, 93.
(27) Deane, R.; Wu, Z.; Zlokovic, B. V. RAGE (Yin) versus LRP (Yang) Balance Regulates Alzheimer Amyloid β-Peptide Clearance Through Transport Across the Blood−Brain Barrier. *Stroke* **2004**, *35*, 2628−2631.
(28) Deane, R.; Du Yan, S.; Submamaryan, R. K.; LaRue, B.; Jovanovic, S.; Hogg, E.; Welch, D.; Manness, L.; Lin, C.; Yu, J.; Zhu, H.; Ghiso, J.; Frangione, B.; Stern, A.; Schmidt, A. M.; Armstrong, D. L.; Arnold, B.; Liliensiek, B.; Nawroth, P.; Hofman, F.; et al. RAGE Mediates Amyloid-β Peptide Transport Across the Blood-Brain Barrier and Accumulation in Brain. *Nature Medicine* **2003**, *9* (7), 907−913.
(29) Wan, W.; Cao, L.; Liu, L.; Zhang, C.; Kalionis, B.; Tai, X.; Li, Y.; Xia, S. Aβ1−42 Oligomer-Induced Leakage in an *in Vitro* Blood−Brain Barrier Model is Associated with Up-Regulation of RAGE and Metalloproteinases, and Down-Regulation of Tight Junction Scaffold Proteins. *Journal of neurochemistry* **2015**, *134* (2), 382−393.
(30) Boado, R. J.; Li, J. Y.; Nagaya, M.; Zhang, C.; Pardridge, W. M. Selective Expression of the Large Neutral Amino Acid Transporter at the Blood−Brain Barrier. *Proc. Natl. Acad. Sci. U. S. A.* **1999**, *96* (21), 12079.
(31) Johnsen, K. B.; Burkhart, A.; Melander, F.; Kempen, P. J.; Vejlebo, J. B.; Siupka, P.; Nielsen, M. S.; Andresen, T. L.; Moos, T. Targeting Transferrin Receptors at the Blood-Brain Barrier Improves the Uptake of Immunoliposomes and Subsequent Cargo Transport into the Brain Parenchyma. *Sci. Rep* **2017**, *7* (1), 10396.
(32) Lajoie, J. M.; Shusta, E. V. Targeting Receptor-Mediated Transport for Delivery of Biologics Across the Blood-Brain Barrier. *Annual review of pharmacology and toxicology* **2015**, *55*, 613−631.
(33) Zhang, F.; Xu, C.-L.; Liu, C.-M. Drug Delivery Strategies to Enhance the Permeability of the Blood−Brain Barrier for Treatment of Glioma. *Drug Design, Development and Therapy* **2015**, *9*, 2089−2100.
(34) Ulbrich, K.; Hekmatara, T.; Herbert, E.; Kreuter, J. Transferrin- and Transferrin-Receptor-Antibody-Modified Nanoparticles Enable Drug Delivery Across the Blood−Brain Barrier (BBB). *Eur. J. Pharm. Biopharm.* **2009**, *71* (2), 251−256.
(35) Tian, X.; Nyberg, S.; Sharp, P. S.; Madsen, J.; Daneshpour, N.; Armes, S. P.; Berwick, J.; Azzouz, M.; Shaw, P.; Abbott, N. J.; Battaglia, G. LRP-1-Mediated Intracellular Antibody Delivery to the Central Nervous System. *Sci. Rep* **2015**, *5*, 11990.
(36) Ong, Z. Y.; Chen, S.; Nabavi, E.; Regoutz, A.; Payne, D. J.; Elson, D. S.; Dexter, D. T.; Dunlop, I. E.; Porter, A. E. Multibranched Gold Nanoparticles with Intrinsic LAT-1 Targeting Capabilities for Selective Photothermal Therapy of Breast Cancer. *ACS Appl. Mater. Interfaces* **2017**, *9* (45), 39259−39270.
(37) Geier, E. G.; Schlessinger, A.; Fan, H.; Gable, J. E.; Irwin, J. J.; Sali, A.; Giacomini, K. M. Structure-Based Ligand Discovery for the Large-neutral Amino Acid Transporter 1, LAT-1. *Proc. Natl. Acad. Sci. U. S. A.* **2013**, *110* (14), 5480−5485.
(38) Marco, S.; Skaper, S. D. Amyloid β-Peptide1−42 Alters Tight Junction Protein Distribution and Expression in Brain Microvessel Endothelial Cells. *Neuroscience letters* **2006**, *401* (3), 219−224.
(39) Yamazaki, Y.; Shinohara, M.; Shinohara, M.; Yamazaki, A.; Murray, M. E.; Liesinger, A. M.; Heckman, M. G.; Lesser, E. R.; Parisi, J. E.; Petersen, R. C. Selective Loss of Cortical Endothelial Tight Junction Proteins During Alzheimer's Disease Progression. *Brain* **2019**, *142* (4), 1077−1092.
(40) Israel, L. L.; Braubach, O.; Galstyan, A.; Chiechi, A.; Shatalova, E. S.; Grodzinski, Z.; Ding, H.; Black, K. L.; Ljubimova, J. Y.; Holler, E. A Combination of Tri-Leucine and Angiopep-2 Drives a Poly-Anionic Polymalic Acid Nanodrug Platform Across the Blood-Brain Barrier. *ACS Nano* **2019**, *13* (2), 1253−1271.
(41) Galstyan, A.; Markman, J. L.; Shatalova, E. S.; Chiechi, A.; Korman, A. J.; Patil, R.; Klymyshyn, D.; Tourtellotte, W. G.; Israel, L. L.; Braubach, O.; Ljubimov, V. A.; Mashouf, L. A.; Ramesh, A.; Grodzinski, Z. B.; Penichet, M. L.; Black, K. L.; Holler, E.; Sun, T.; Ding, H.; Ljubimov, A. V.; et al. Blood−Brain Barrier Permeable Nano Immunoconjugates Induce Local Immune Responses for Glioma Therapy. *Nat. Commun.* **2019**, *10* (1), 3850.
(42) Ding, H.; Portilla-Aries, J.; Patil, R.; Black, K. L.; Ljubimova, J. Y.; Holler, E. Polymalic Acid Peptide Copolymers: Design and Optimization for Endosomolytic Drug Delivery. *Biomaterials* **2011**, *32*, 5269−5278.
(43) Ding, H.; Portilla-Arias, J.; Patil, R.; Black, K. L.; Ljubimova, J. Y.; Holler, E. Distinct Mechanisms of Membrane Permeation Induced by Two Polymalic Acid Copolymers. *Biomaterials* **2013**, *34*, 217−225.
(44) Ljubimova, J. Y.; Portilla-Arias, J.; Patil, R.; Ding, H.; Inoue, S.; Markman, J. L.; Rekechenetskiy, A.; Konda, B.; Gangalum, P. R.; Chesnokova, A.; Ljubimov, A. V.; Black, K. L.; Holler, E. Toxicity and Efficacy Evaluation of Multiple Targeted Polymalic Acid Conjugates for Triple-Negative Breast Cancer Treatment. *J. Drug Targeting* **2013**, *21* (10), 956−967.
(45) Demeule, M.; Regina, A.; Che, C.; Poirier, J.; Nguyen, T.; Gabathuler, R.; Castaigne, J.-P.; Beliveau, R. Identification and Design of Peptides as a New Drug Delivery System for the Brain. *Journal of Pharmacology and Experimental Therapeutics* **2008**, *324* (3), 1064−1072.
(46) Demeule, M.; Currie, J. C.; Bertrand, Y.; Che, C.; Nguyen, T.; Regina, A.; Gabathuler, R.; Castaigne, J. P.; Beliveau, R. Involvement of the Low-Density Lipoprotein Receptor-Related Protein in the Transcytosis of the Brain Delivery Vector Angiopep-2. *Journal of neurochemistry* **2008**, *106* (4), 1534−1544.
(47) Demeule, M.; Beaudet, N.; Régina, A.; Besserer-Offroy, É.; Murza, A.; Tétreault, P.; Belleville, K.; Ché, C.; Larocque, A.; Thiot, C. Conjugation of a Brain-Penetrant Peptide with Neurotensin Provides Antinociceptive Properties. *J. Clin. Invest.* **2014**, *124* (3), 1199.

(48) Molino, Y.; David, M.; Varini, K.; Jabès, F.; Gaudin, N.; Fortoul, A.; Bakloul, K.; Masse, M.; Bernard, A.; Drobecq, L. Use of LDL Receptor−Targeting Peptide Vectors for *in Vitro* and *in Vivo* Cargo Transport Across the Blood-Brain Barrier. *FASEB J.* **2017**, *31* (5), 1807−1827.
(49) Morales-Zavala, F.; Arriagada, H.; Hassan, N.; Velasco, C.; Riveros, A.; Álvarez, A. R.; Minniti, A. N.; Rojas-Silva, X.; Muñoz, L. L.; Vasquez, R. Peptide Multifunctionalized Gold Nanorods Decrease Toxicity of β-Amyloid Peptide in a Caenorhabditis Elegans Model of Alzheimer's Disease. *Nanomedicine: Nanotechnology, Biology and Medicine* **2017**, *13* (7), 2341−2350.
(50) Eggert, S.; Thomas, C.; Kins, S.; Hermey, G. Trafficking in Alzheimer's Disease: Modulation of APP Transport and Processing by the Transmembrane Proteins LRP1, SorLA, SorCS1c, Sortilin, and Calsyntenin. *Molecular neurobiology* **2018**, *55* (7), 5809−5829.
(51) Wang, R.; Wang, C.; Dai, Z.; Chen, Y.; Shen, Z.; Xiao, G.; Chen, Y.; Zhou, J.-N.; Zhuang, Z.; Wu, R. An Amyloid-β Targeting Chemical Exchange Saturation Transfer Probe for In Vivo Detection of Alzheimer's Disease. *ACS Chem. Neurosci.* **2019**, *10* (8), 3859−3867.
(52) Van Groen, T.; Kadish, I.; Wiesehan, K.; Funke, S. A.; Willbold, D. *In Vitro* and *in Vivo* Staining Characteristics of Small, Fluorescent, Abeta-42-Binding D-Enantiomeric Peptides in Transgenic AD Mouse Models. *ChemMedChem.* **2009**, *4* (2), 276−82.
(53) Funke, S. A.; van Groen, T.; Kadish, I.; Bartnik, D.; Nagel-Steger, L.; Brener, O.; Sehl, T.; Batra-Safferling, R.; Moriscot, C.; Schoehn, G. Oral Treatment with the D-Enantiomeric Peptide D3 Improves the Pathology and Behavior of Alzheimer's Disease Transgenic Mice. *ACS chemical neuroscience* **2010**, *1* (9), 639−648.
(54) Wiesehan, K.; Buder, K.; Linke, R. P.; Patt, S.; Stoldt, M.; Unger, E.; Schmitt, B.; Bucci, E.; Willbold, D. Selection of D-amino-Acid Peptides that Bind to Alzheimer's Disease Amyloid Peptide abeta1−42 by Mirror Image Phage Display. *Chembiochem: a European journal of chemical biology* **2003**, *4* (8), 748−53.
(55) Van Groen, T.; Wiesehan, K.; Funke, S. A.; Kadish, I.; Nagel-Steger, L.; Willbold, D. Reduction of Alzheimer's Disease Amyloid Plaque Load in Transgenic Mice by D3, ad-Enantiomeric Peptide Identified by Mirror Image Phage Display. *ChemMedChem: Chemistry Enabling Drug Discovery* **2008**, *3* (12), 1848−1852.
(56) Funke, S. A.; Bartnik, D.; Glück, J. M.; Piorkowska, K.; Wiesehan, K.; Weber, U.; Gulyas, B.; Halldin, C.; Pfeifer, A.; Spenger, C. Development of a Small D-Enantiomeric Alzheimer's Amyloid-β Binding Peptide Ligand for Future *in Vivo* Imaging Applications. *PloS one* **2012**, *7* (7), No. e41457.
(57) Xia, H.; Anderson, B.; Mao, Q.; Davidson, B. L. Recombinant Human Adenovirus: Targeting to the Human Transferrin Receptor Improves Gene Transfer to Brain Microcapillary Endothelium. *Journal of virology* **2000**, *74* (23), 11359−11366.
(58) Yin, T.; Yang, L.; Liu, Y.; Zhou, X.; Sun, J.; Liu, J. Sialic Acid (SA)-Modified Selenium Nanoparticles Coated with a High Blood−Brain Barrier Permeability Peptide-B6 Peptide for Potential Use in Alzheimer's Disease. *Acta biomaterialia* **2015**, *25*, 172−183.
(59) Georgieva, J. V.; Hoekstra, D.; Zuhorn, I. S. Smuggling Drugs into the Brain: an Overview of Ligands Targeting Transcytosis for Drug Delivery Across the Blood−Brain Barrier. *Pharmaceutics* **2014**, *6* (4), 557−583.
(60) Smith, N. D. S. Protein Engineering for Receptor-Mediated Drug Delivery Across the Blood-Brain Barrier; Honors Project; Smith College, Northampton, MA. 2016.
(61) Yu, Y. J.; Atwal, J. K.; Zhang, Y.; Tong, R. K.; Wildsmith, K. R.; Tan, C.; Bien-Ly, N.; Hersom, M.; Maloney, J. A.; Meilandt, W. J. Therapeutic Bispecific Antibodies Cross the Blood-Brain Barrier in Nonhuman Primates. *Science translational medicine* **2014**, *6* (261), 261ra154−261ra154.
(62) Oller-Salvia, B.; Sánchez-Navarro, M.; Ciudad, S.; Guiu, M.; Arranz-Gibert, P.; Garcia, C.; Gomis, R. R.; Cecchelli, R.; García, J.; Giralt, E. MiniAp-4: a Venom-Inspired Peptidomimetic for Brain Delivery. *Angew. Chem., Int. Ed.* **2016**, *55* (2), 572−575.
(63) Oller-Salvia, B.; Teixidó, M.; Giralt, E. From Venoms to BBB Shuttles: Synthesis and Blood−Brain Barrier Transport Assessment of Apamin and a Nontoxic Analog. *Peptide Science* **2013**, *100* (6), 675−686.
(64) Wehbe, R.; Frangieh, J.; Rima, M.; El Obeid, D.; Sabatier, J.-M.; Fajloun, Z. Bee Venom: Overview of Main Compounds and Bioactivities for Therapeutic Interests. *Molecules* **2019**, *24* (16), 2997.
(65) Moreno, M.; Giralt, E. Three Valuable Peptides from Bee and Wasp Venoms for Therapeutic and Biotechnological Use: Melittin, Apamin and Mastoparan. *Toxins* **2015**, *7* (4), 1126−1150.
(66) Fuster, C.; Varese, M.; García, J.; Giralt, E.; Sánchez-Navarro, M.; Teixidó, M. Expanding the MiniAp-4 BBB-Shuttle Family: Evaluation of Proline cis-trans Ratio as Tool to Fine-Tune Transport. *Journal of Peptide Science* **2019**, *25* (5), No. e3172.
(67) Dal Magro, R.; Simonelli, S.; Cox, A.; Formicola, B.; Corti, R.; Cassina, V.; Nardo, L.; Mantegazza, F.; Salerno, D.; Grasso, G.; Deriu, M. A.; Danani, A.; Calabresi, L.; Re, F. The Extent of Human Apolipoprotein A-I Lipidation Strongly Affects the β-Amyloid Efflux Across the Blood-Brain Barrier *in Vitro*. *Frontiers in Neuroscience* **2019**, *13* (419), 1 DOI: 10.3389/fnins.2019.00419.
(68) Liu, H.; Funke, S. A.; Willbold, D. Transport of Alzheimer Disease Amyloid-β-Binding d-Amino Acid Peptides Across an *in Vitro* Blood−Brain Barrier Model. *Rejuvenation research* **2010**, *13* (2−3), 210−213.
(69) Sakamoto, K.; Shinohara, T.; Adachi, Y.; Asami, T.; Ohtaki, T. A Novel LRP1-Binding Peptide L57 that Crosses the Blood Brain Barrier. *Biochemistry and biophysics reports* **2017**, *12*, 135−139.
(70) Fernandes, J.; Ghate, M. V.; Basu Mallik, S.; Lewis, S. A. Amino Acid Conjugated Chitosan Nanoparticles for the Brain Targeting of a Model Dipeptidyl Peptidase-4 Inhibitor. *Int. J. Pharm.* **2018**, *547* (1), 563−571.
(71) Gonzalez-Carter, D. A.; Ong, Z. Y.; McGilvery, C. M.; Dunlop, I. E.; Dexter, D. T.; Porter, A. E. L-DOPA Functionalized, Multi-branched Gold Nanoparticles as Brain-Targeted Nano-Vehicles. *Nanomedicine: Nanotechnology, Biology and Medicine* **2019**, *15* (1), 1−11.
(72) Li, L.; Di, X.; Wu, M.; Sun, Z.; Zhong, L.; Wang, Y.; Fu, Q.; Kan, Q.; Sun, J.; He, Z. Targeting Tumor Highly-Expressed LAT1 Transporter with Amino Acid-Modified Nanoparticles: Toward a Novel Active Targeting Strategy in Breast Cancer Therapy. *Nanomedicine: Nanotechnology, Biology and Medicine* **2017**, *13* (3), 987−998.
(73) Li, L.; Di, X.; Zhang, S.; Kan, Q.; Liu, H.; Lu, T.; Wang, Y.; Fu, Q.; Sun, J.; He, Z. Large Amino Acid Transporter 1 Mediated Glutamate Modified Docetaxel-Loaded Liposomes for Glioma Targeting. *Colloids Surf., B* **2016**, *141*, 260−267.
(74) Takahashi, Y.; Nishimura, T.; Higuchi, K.; Noguchi, S.; Tega, Y.; Kurosawa, T.; Deguchi, Y.; Tomi, M. Transport of Pregabalin Via L-Type Amino Acid Transporter 1 (SLC7A5) in Human Brain Capillary Endothelial Cell Line. *Pharm. Res.* **2018**, *35* (12), 246.
(75) Kenett, R. S. Z.; Amberti, D. *Modern Industrial Statistics: with Applications in R, MINITAB and JMP*, 2nd ed.; John Wiley and Sons: Chichester, 2014.
(76) Kenett, R.; Zacks, S. *Modern Industrial Statistics: Design and Control of Quality and Reliability*; Duxbury press: San Francisco, 1998.
(77) Israel, L. L.; Lellouche, E.; Kenett, R.; Green, O.; Michaeli, S.; Lellouche, J. P. $Ce^{3/4+}$ Cation-Functionalized Maghemite Nanoparticles Towards siRNA-Mediated Gene Silencing. *J. Mater. Chem. B* **2014**, *2* (37), 6215−6225.
(78) Eikelenboom, P.; Van Exel, E.; Hoozemans, J. J.; Veerhuis, R.; Rozemuller, A. J.; Van Gool, W. A. Neuroinflammation−an Early Event in Both the History and Pathogenesis of Alzheimer's Disease. *Neurodegenerative Diseases* **2010**, *7* (1−3), 38−41.
(79) Dickson, T.; Vickers, J. The Morphological Phenotype of β-Amyloid Plaques and Associated Neuritic Changes in Alzheimer's Disease. *Neuroscience* **2001**, *105* (1), 99−107.
(80) Smith, A. D. Imaging the Progression of Alzheimer Pathology Through the Brain. *Proc. Natl. Acad. Sci. U. S. A.* **2002**, *99* (7), 4135−4137.

(81) Frisoni, G. B.; Boccardi, M.; Barkhof, F.; Blennow, K.; Cappa, S.; Chiotis, K.; Démonet, J.-F.; Garibotto, V.; Giannakopoulos, P.; Gietl, A. Strategic Roadmap for an Early Diagnosis of Alzheimer's Disease Based on Biomarkers. *Lancet Neurology* **2017**, *16* (8), 661−676.
(82) Masliah, E.; Mallory, M.; Alford, M.; DeTeresa, R.; Hansen, L.; McKeel, D.; Morris, J. Altered Expression of Synaptic Proteins Occurs Early During Progression of Alzheimer's Disease. *Neurology* **2001**, *56* (1), 127−129.
(83) Bagyinszky, E.; Giau, V. V.; Shim, K.; Suk, K.; An, S. S. A.; Kim, S. Role of Inflammatory Molecules in the Alzheimer's Disease Progression and Diagnosis. *Journal of the neurological sciences* **2017**, *376*, 242−254.
(84) Veitch, D. P.; Weiner, M. W.; Aisen, P. S.; Beckett, L. A.; Cairns, N. J.; Green, R. C.; Harvey, D.; Jack, C. R., Jr; Jagust, W.; Morris, J. C. Understanding Disease Progression and Improving Alzheimer's Disease Clinical Trials: Recent Highlights from the Alzheimer's Disease Neuroimaging Initiative. *Alzheimer's & Dementia* **2019**, *15* (1), 106−152.
(85) Gaugler, J.; James, B.; Johnson, T.; Marin, A.; Weuve, J. 2019 Alzheimer's Disease Facts and Figures. *Alzheimers & Dementia* **2019**, *15* (3), 321−387.
(86) Bourassa, P.; Alata, W.; Tremblay, C.; Paris-Robidas, S.; Calon, F. Transferrin Receptor-Mediated Uptake at the Blood−Brain Barrier Is Not Impaired by Alzheimer's Disease Neuropathology. *Mol. Pharmaceutics* **2019**, *16* (2), 583−594.
(87) Baloyannis, S. Brain Capillaries in Alzheimer's Disease. *Hellenic journal of nuclear medicine* **2015**, *18*, 152.
(88) Kitaguchi, H.; Ihara, M.; Saiki, H.; Takahashi, R.; Tomimoto, H. Capillary Beds are Decreased in Alzheimer's Disease, But Not in Binswanger's Disease. *Neurosci. Lett.* **2007**, *417* (2), 128−131.
(89) Osgood, D.; Miller, M. C.; Messier, A. A.; Gonzalez, L.; Silverberg, G. D. Aging Alters mRNA Expression of Amyloid Transporter Genes at the Blood-Brain Barrier. *Neurobiology of Aging* **2017**, *57*, 178−185.
(90) Krause, G.; Winkler, L.; Mueller, S. L.; Haseloff, R. F.; Piontek, J.; Blasig, I. E. Structure and Function of Claudins. *Biochimica et Biophysica Acta (BBA)-Biomembranes* **2008**, *1778* (3), 631−645.
(91) Krug, S. M.; Günzel, D.; Conrad, M. P.; Lee, I. F. M.; Amasheh, S.; Fromm, M.; Yu, A. S. Charge-Selective Claudin Channels. *Ann. N.Y. Acad. Sci.* **2012**, *1257* (1), 20−28.
(92) Tamura, A.; Hayashi, H.; Imasato, M.; Yamazaki, Y.; Hagiwara, A.; Wada, M.; Noda, T.; Watanabe, M.; Suzuki, Y.; Tsukita, S. Loss of Claudin-15, But Not Claudin-2, Causes Na+ Deficiency and Glucose Malabsorption in Mouse Small Intestine. *Gastroenterology* **2011**, *140* (3), 913−923.
(93) Weizmann Institute of Science. *GeneCards® The human gene database*; https://www.genecards.org/cgi-bin/carddisp.pl?gene=CLDN18, Version 5.9, last accesed 2022−05−17.
(94) Abadier, M.; Lyck, R., Pathways Across the Blood-Brain Barrier. In *The Blood Brain Barrier and Inflammation*, Lyck, R.; Enzmann, G., Eds.; Springer International Publishing: Cham, 2017; pp 187−211.
(95) Weizmann Institute of Science. *PathCards Pathway Unification Database*; https://pathcards.genecards.org, Version 5.7.551.0, Updated 2021−12−21, last accesed 2022−05−17.
(96) Merico, D.; Gfeller, D.; Bader, G. D. How to Visually Interpret Biological Data Using Networks. *Nature biotechnology* **2009**, *27* (10), 921−924.
(97) Lue, L.-F.; Pai, M.-C.; Chen, T.-F.; Hu, C.-J.; Huang, L.-K.; Lin, W.-C.; Wu, C.-C.; Jeng, J.-S.; Blennow, K.; Sabbagh, M. N.; Yan, S.-H.; Wang, P.-N.; Yang, S.-Y.; Hatsuta, H.; Morimoto, S.; Takeda, A.; Itoh, Y.; Liu, J.; Xie, H.; Chiu, M.-J. Age-Dependent Relationship Between Plasma Aβ40 and Aβ42 and Total Tau Levels in Cognitively Normal Subjects. *Frontiers in Aging Neuroscience* **2019**, *11* (222), 1 DOI: 10.3389/fnagi.2019.00222.
(98) Mehta, P. D.; Pirttila, T.; Mehta, S. P.; Sersen, E. A.; Aisen, P. S.; Wisniewski, H. M. Plasma and Cerebrospinal Fluid Levels of Amyloid Beta Proteins 1−40 and 1−42 in Alzheimer Disease. *Archives of neurology* **2000**, *57* (1), 100−5.
(99) Hladky, S. B.; Barrand, M. A. Elimination of Substances from the Brain Parenchyma: Efflux *via* Perivascular Pathways and *via* the Blood−Brain Barrier. *Fluids and Barriers of the CNS* **2018**, *15* (1), 30.
(100) Dehouck, B.; Dehouck, M. P.; Fruchart, J. C.; Cecchelli, R. Upregulation of the Low Density Lipoprotein Receptor at the Blood-Brain Barrier: Intercommunications Between Brain Capillary Endothelial Cells and Astrocytes. *J. Cell Biol.* **1994**, *126* (2), 465−473.
(101) Gosselet, F.; Candela, P.; Sevin, E.; Berezowski, V.; Cecchelli, R.; Fenart, L. Transcriptional Profiles of Receptors and Transporters Involved in Brain Cholesterol Homeostasis at the Blood−Brain Barrier: Use of an *in Vitro* Model. *Brain Res.* **2009**, *1249*, 34−42.
(102) Candela, P.; Saint-Pol, J.; Kuntz, M.; Boucau, M.-C.; Lamartiniere, Y.; Gosselet, F.; Fenart, L. *In Vitro* Discrimination of the Role of LRP1 at the BBB Cellular Level: Focus on Brain Capillary Endothelial Cells and Brain Pericytes. *Brain Res.* **2015**, *1594*, 15−26.
(103) Tian, X.; Leite, D. M.; Scarpa, E.; Nyberg, S.; Fullstone, G.; Forth, J.; Matias, D. L.; Apriceno, A.; Poma, A.; Duro-Castano, A.; Vuyyuru, M.; Harker-Kirschneck, L.; Šarić, A.; Zhang, Z.; Xiang, P.; Fang, B.; Tian, Y.; Luo, L.; Rizzello, L.; Battaglia, G. On the shuttling across the blood-brain barrier via tubule formation: Mechanism and cargo avidity bias. *Sci. Adv.* **2020**, *6* (48), No. abc4397.
(104) Cho, C. F.; Wolfe, J. M.; Fadzen, C. M.; Calligaris, D.; Hornburg, K.; Chiocca, E. A.; Agar, N. Y. R.; Pentelute, B. L.; Lawler, S. E. Blood-Brain-Barrier Spheroids as an *in Vitro* Screening Platform for Brain-Penetrating Agents. *Nat. Commun.* **2017**, *8*, 15623.
(105) Di Guardo, G. Lipofuscin, Lipofuscin-Like Pigments and Autofluorescence. *European Journal of Histochemistry: EJH* **2015**, *59* (1), 2485.
(106) Feldman, T. B.; Yakovleva, M. A.; Dontsov, A. E.; Ostrovsky, M. A. Fluorescence Emission and Excitation Spectra of Fluorophores of Lipofuscin Granules Isolated from Retinal Pigment Epithelium of Human Cadaver Eyes. *Russian Chemical Bulletin* **2010**, *59* (1), 276−283.
(107) Marmorstein, A. D.; Marmorstein, L. Y.; Sakaguchi, H.; Hollyfield, J. G. Spectral Profiling of Autofluorescence Associated with Lipofuscin, Bruch's Membrane, and Sub-RPE Deposits in Normal and AMD Eyes. *Investigative Ophthalmology & Visual Science* **2002**, *43* (7), 2435−2441.